



Fractional melting and smelting on the ureilite parent body

Cyrena Anne Goodrich^{a,*}, James A. Van Orman^b, Lionel Wilson^{c,d}

^a *Department of Physical Sciences, Kingsborough Community College, 2001 Oriental Blvd, Brooklyn, NY 11235, USA*

^b *Department of Geological Sciences, Case Western Reserve University, Cleveland, OH 44106, USA*

^c *Environmental Science Department, Institute of Environmental and Natural Sciences, Lancaster University, Lancaster LA1 4YQ, UK*

^d *Hawaii Institute of Geophysics and Planetology, School of Ocean and Earth Science and Technology, University of Hawaii at Manoa, Honolulu, HI 96822, USA*

Received 19 July 2006; accepted in revised form 19 March 2007; available online 3 April 2007

Abstract

We investigate petrologic and physical aspects of melt extraction on the parent asteroid of the ureilite meteorites (UPB). We first develop a petrologic model for simultaneous melting and smelting (reduction of FeO by C) at various depths. For a model starting composition, determined from petrologic constraints to have been CV-like except for elevated Ca/Al ($2.5 \times \text{CI}$), we determine (1) degree of melting, (2) the evolution of *mg*, (3) production of CO + CO₂ gas and (4) the evolution of mineralogy in the residue as a function of temperature and pressure. We then use these relationships to examine implications of fractional vs. batch melt extraction.

In the shallowest source regions (~ 30 bars), melting and smelting begin simultaneously at ~ 1050 °C, so that *mg* and the abundance of low-Ca pyroxene (initially pigeonite, ultimately pigeonite + orthopyroxene) begin to increase immediately. However, in the deepest source regions (~ 100 bars), smelting does not begin until ~ 1200 °C, so that *mg* begins to increase and low-Ca pyroxene (pigeonite) appears only after $\sim 21\%$ melting. The final residues in these two cases, obtained just after the demise of augite, match the end-members of the ureilite *mg* range (~ 94 – 76) in pyroxene abundance and type. In all source regions, production of CO + CO₂ by smelting varies over the course of melting. The onset of smelting results in a burst of gas production and very high incremental gas/melt ratios (up to ~ 2.5 by mass); after a few % (s)melting, however, these values drastically decline (to < 0.05 in the final increments).

Physical modelling based on these relationships indicates that melts would begin to migrate upwards after only ~ 1 – 2% melting, and thereafter would migrate continuously (fractionally) and rapidly (reaching the surface in < 1 year) in a network of veins/dikes. All melts produced during the smelting stage in each source region have gas contents sufficient to cause them to erupt explosively and be lost. However, since in all but the shallowest source regions part of the melting sequence occurs without smelting, fractional melting implies that a significant fraction of UPB melts may have erupted more placidly to form a thin crust (~ 3.3 km thick for a 100 km radius body).

Our calculations suggest that melt extraction was so rapid that equilibrium trace element partitioning may not have been attained. We present a model for disequilibrium fractional melting (in which REE partitioning is limited by diffusion) on the UPB, and demonstrate that it produces a good match to the ureilite data. The disequilibrium model may also apply to trace siderophile elements, and might help explain the “overabundance” of these elements in ureilites relative to predictions from the smelting model.

Our results suggest that melt extraction on the UPB was a rapid, fractional process, which can explain the preservation of a primitive oxygen isotopic signature on the UPB.

© 2007 Elsevier Ltd. All rights reserved.

* Corresponding author.

E-mail address: cgoodrich@kingsborough.edu (C.A. Goodrich).

1. INTRODUCTION

The ureilites, which form the second largest group of achondrites (~210 recognized samples), are coarse-grained, highly equilibrated ultramafic (olivine–pyroxene) rocks thought to represent the mantle of a partially melted, carbon-rich asteroid (Goodrich, 1992; Mittlefehldt et al., 1998; Goodrich et al., 2004). Intriguingly, although they show clear evidence of high-temperature (1100–1300 °C) igneous processing, they also show primitive oxygen isotopic characteristics. Thus, they may preserve a unique stage or mode of early planetary differentiation.

Monomict ureilites can be divided into three types, based on the identity of their pyroxenes (Goodrich et al., 2004, 2006). Olivine–pigeonite ureilites (the most abundant) contain uninverted pigeonite ($Wo \sim 7$ –13) as their main (usually sole) pyroxene, and span a large range of mg ($Fo \sim 76$ –87). Olivine–orthopyroxene ureilites (Table 1) contain orthopyroxene ($Wo \leq 5$) instead of, or in addition to, pigeonite, and have highly magnesian compositions ($Fo \sim 86$ –92). Together, these two groups define a single Fe/Mg–Fe/Mn trend of near-constant, chondritic Mn/Mg, which suggests that they are residues (consistent with their equilibrated textures) and are related to one another by various degrees of reduction of common precursor material (Goodrich and Delaney, 2000). The relatively rare augite-bearing ureilites have variously higher Mn/Mg ratios which suggest that they are cumulates (consistent with their poikilitic textures and the presence of melt inclusions), but show the same large range in degree of reduction (Fo 76–95). The reduction relationship among ureilites can be explained by smelting (the metallurgical term for reduction of metallic ore by carbon) over a range of pressures (hence depths) in the ureilite parent body (Fig. 1), an interpretation that is supported by a correlation between Fo and pyroxene/olivine ratio and by the restriction of orthopyroxene to the most magnesian compositions (Fig. 2). Ureilite smelting pressures have been estimated to range from ~5 to 30 bars for the most ferroan ureilite to ~50–125 bars for the most magnesian (Berkley and Jones, 1982; Goodrich et al., 1987; Warren and Kallemeyn, 1992; Walker and Grove, 1993; Sinha et al., 1997; Singletary and Grove, 2003). The latter imply a minimum size for the ureilite parent body (UPB) of ~100 km in radius.

Table 1
Olivine–orthopyroxene ureilites^a

Name/pairings	Fo	Orthopyroxene (%)	Pigeonite (%)	References
EET 87517 ^b	92.3	55	—	1, 2
EET 96262/96322/96328/ 87511/87523/87717	87.1	45	—	2
LEW 85440/88201/ 88102/88281	91.2	42–46	—	2, 3
Y 74659	91.8	3	52	3
Y 791538	91.4	18–20	27–28	2, 3

References: (1) Singletary and Grove (2003); (2) this work; (3) Takeda (1989).

^a Includes all olivine–orthopyroxene ureilites for which adequate descriptions currently exist. Several recently discovered samples (Russell et al., 2004, 2005) may also belong to this group.

^b This ureilite was classified by Singletary and Grove (2003) as olivine–pigeonite. However, because of the low Wo content (4.5) and optical properties of its low-Ca pyroxene, we classify it as olivine–orthopyroxene.

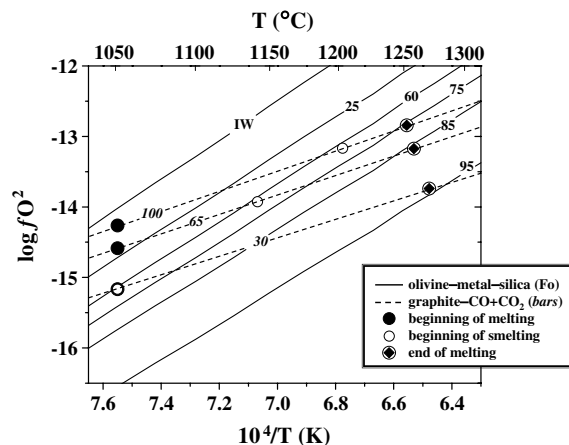


Fig. 1. Plot of $\log fO_2$ vs. T , showing curves of graphite–CO + CO₂ equilibrium at 30, 65 and 100 bars total gas pressure and of olivine–silica–metal equilibrium at various Fo values. Equilibration temperatures in the range of ~1250–1275 °C for ureilites ($Fo \sim 76$ –94) indicate that they are derived from pressures of ~30–100 bars. Assuming a bulk ureilite parent body (UPB) with a total iron content similar to that of Allende ($mg \sim 62$, if all iron occurs as FeO), silicate melting begins at ~1050 °C (solid circles). Smelting begins when the value of Fo buffered by carbon redox equilibrium exceeds 62. The temperature at which this occurs (open circles) depends on pressure (depth). At 30 bars, smelting begin approximately simultaneously with melting; however, at 100 bars, it does not begin until T reaches nearly 1200 °C. Note that at depths corresponding to pressures greater than ~100–125 bars (and high magmatic temperatures), smelting does not occur on the UPB because carbon redox equilibria buffer Fo values lower than those of the starting material. IW = iron–wüstite buffer. Graphite–CO + CO₂ equilibria calculated using the precise thermodynamical treatment of French and Eugster (1965). Olivine–silica–metal (OSI) equilibria calculated from the equations of Nitsan (1974) and Williams (1972).

From the point of view of planetary differentiation, what is missing from this picture is the basaltic (crustal) complement to these ultramafic (mantle) rocks—i.e. the melts. Warren and Kallemeyn (1992) and Scott et al. (1993) suggested that the absence of basaltic ureilites could be explained if melts generated on the UPB had high contents of CO + CO₂ gas derived from smelting, and therefore erupted explosively (Wilson and Keil, 1991) at velocities sufficient to escape their parent and be lost. If this is the

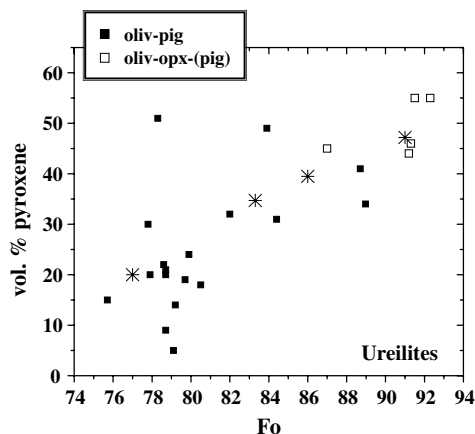


Fig. 2. Relationship between Fo content of olivine and modal abundance of pyroxene in olivine + low-Ca pyroxene ureilites. Positive correlation supports the model that *mg* was determined by pressure-dependent carbon redox control (smelting) on the UPB. Asterisks represent results from MAGPOX calculations for model ureilite precursor material used in this study. Data for olivine–pigeonite ureilites from Singletary and Grove (2003). Data for olivine–orthopyroxene ureilites from Takeda (1989) and this work (Table 1). One ureilite (EET 87517) classified as olivine–pigeonite by Singletary and Grove (2003) has been reclassified here as olivine–orthopyroxene (on the basis of the low *Wo* content and optical characteristics of the pyroxene).

case, then the UPB may never have had a crust. Nevertheless, some insights into the nature of melts on the UPB have been gleaned from polymict ureilites, which are regolith breccias and contain a few percent of feldspathic clasts (Goodrich et al., 2004). Detailed studies of these clasts (e.g. Ikeda et al., 2000; Ikeda and Prinz, 2001; Cohen et al., 2004) have identified several feldspathic igneous lithologies that may represent melts complementary to the monomict ureilites. Interestingly, the compositions of these lithologies (none of which is basaltic), suggest that melt extraction on the UPB may have been a fractional, rather than batch, process (Cohen et al., 2004; Goodrich et al., 2004; Kita et al., 2004).

This conclusion would be highly significant, in that it might explain the preservation of a primitive oxygen isotopic signature on the UPB. The oxygen isotopic compositions of ureilites define a $\delta^{17}\text{O}$ – $\delta^{18}\text{O}$ line of slope ~ 1 , nearly coincident with the CCAM line (Clayton and Mayeda, 1988, 1996). This pattern is remarkable, as most other achondrites show $\delta^{17}\text{O}$ – $\delta^{18}\text{O}$ trends of slope $\sim 1/2$, reflecting isotopic homogenization and mass-dependent fractionation as expected from igneous processing. Furthermore, $\Delta^{17}\text{O}$ values are correlated with *mg* (or Fo), which in the smelting model implies a correlation with depth (Walker and Grove, 1993; Goodrich et al., 2002). The preservation of such a correlation (depth gradient) during high-*T* igneous processing seems unlikely, but it may be explained if melt extraction was a rapid, fractional process in which the melts did not interact substantially with the rocks through which they migrated.

The focus of this paper is to investigate whether melt extraction on the UPB could have been fractional. We

begin by examining the chemical/mineralogical composition of ureilite precursor material, and then develop a petrologic model for simultaneous melting and smelting of this material at various depths. Previous studies have addressed the final products of smelting (i.e. the ureilitic residues), but have not considered how smelting progresses during the course of melting. This may be critical if melting was fractional. Specifically, we determine (1) degree of melting, (2) the evolution of *mg*, (3) production of CO + CO₂ gas and (4) the evolution of mineralogy in the residue as a function of temperature (during heating) and pressure. We then use these relationships to examine implications of batch vs. fractional melting, and to test which of these occurred. In particular, we model the physics (mode and rate) of melt extraction, and the partitioning of rare earth element (REE) on the UPB.

2. COMPOSITION OF UREILITE PRECURSOR MATERIALS

In order to model melt generation and extraction on the UPB, we must know the chemical/mineralogical composition of the starting material. Most models for the petrogenesis of ureilites have assumed carbonaceous chondrite-like precursors, as suggested by their oxygen isotopic compositions (which specifically point toward CV-like material) and their high carbon contents (Mittlefehldt et al., 1998). Although in detail the data (e.g. carbon isotopic compositions: Grady et al., 1985) do not show a clear link to any specific carbonaceous chondrite group, this remains the most reasonable assumption. Goodrich (1999) examined anhydrous chondritic silicate compositions with respect to their ability to produce ureilites (i.e. their major mineral assemblages) as residues of batch melting. This modelling, which utilized the melting/crystallization program MAGPOX (Longhi, 1991) showed that strictly chondritic compositions (when reduced to the *mg* range of ureilites) cannot produce olivine–pigeonite residues; they produce exclusively olivine–orthopyroxene residues. Investigation of the effects of key compositional parameters in the orthopyroxene–plagioclase–wollastonite (Opx–Plag–Wo) phase system (Fig. 3) led to the conclusion that ureilite precursor materials must have had (1) Ca/Al ratios of 2–3.5 × CI; (2) very low alkali contents (similar to the lowest in the carbonaceous chondrite range); (3) various Al/Mg ratios (~ 0.75 – $1.25 \times \text{CI}$); and (4) Si/Mg ratio similar to that of ordinary ($\sim 1.15 \times \text{CI}$), rather than carbonaceous chondrites.

Recently, some of these conclusions were challenged by Kita et al. (2004). These authors performed partial melting calculations using MELTS (Ghiorso and Sack, 1995), and reported that batch melting of anhydrous silicate CM reduced to *mg* 77 (low end of the ureilite *mg* range) produced an olivine–pigeonite residue, a result that is not in agreement with the MAGPOX calculations (Fig. 3). They also suggested that fractional (as opposed to batch) melting of chondritic materials might have led to increasingly superchondritic Ca/Al ratios in residues and thus pigeonite-bearing residues. In addition, their trace element (K, Ba, Sr) modelling suggested that feldspathic materials in polymict ureilites (assumed to represent UPB melts) were produced

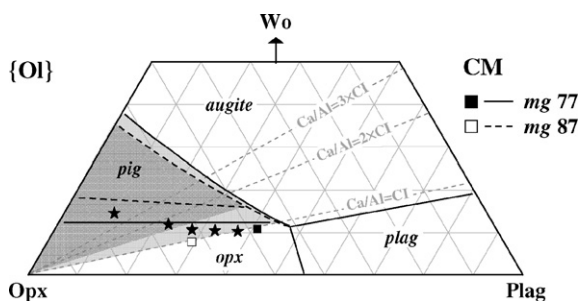


Fig. 3. Orthopyroxene–plagioclase–wollastonite (Opx–Plag–Wo) phase system projected from olivine (Ol), showing bulk composition of anhydrous silicate CM, reduced to *mg* 77 and *mg* 87, (~ the range of olivine–pigeonite ureilites (*mg* of bulk compositions and Fo of olivine in final residue are nearly the same). Locations of phase boundaries are dependent on *mg* and alkali contents; those shown (calculated with MAGPOX) are specific to CM at low degrees of melting. Light grey and dark grey shaded areas show, for *mg* 77 and *mg* 87, respectively, the region in which a bulk composition must plot in order to produce an olivine–pigeonite residue. Comparison of these regions with loci of constant Ca/Al shows that this requirement is best met by compositions with superchondritic Ca/Al. Black stars are data from Kita et al. (2004) showing calculated compositions of residues produced in progressive fractional melting (up to ~23%) of CM at *mg* 77. Note that, although the Ca/Al ratios of these residues increase as a result of fractionation, they do not move into the pigeonite field, and thus a ureilite-like final assemblage is not produced. See Longhi (1991) for projection equations.

from alkali-undepleted materials. Here we examine these suggestions and reevaluate the conclusions of Goodrich (1999).

First, we have investigated batch melting of CM at *mg* 77 using both MAGPOX and MELTS, in order to examine discrepancies between the programs. We have been working with John Longhi to improve the parameterization of the orthopyroxene–pigeonite phase boundary in MAGPOX by comparison to experimental studies (Longhi and Pan, 1988; Grove and Juster, 1989; Singletary and Grove, 2003), and are using a recent version that incorporates these revisions. The melting sequence derived from our MELTS calculation (Fig. 4a) is in agreement with the results of Kita et al. (2004) up until ~23% melting—the point at which plagioclase is eliminated and an olivine + low-Ca pyroxene residue is produced. Our calculations shows that at this point, pigeonite ($Wo \sim 14$) is replaced by orthopyroxene ($Wo \sim 5$), which implies a configuration of phase boundaries in the Opx–Plag–Wo system such as that shown on the right in Fig. 4a, and an olivine–orthopyroxene residue is produced. In contrast, Kita et al. (2004) report no change in pyroxene identity, and hence conclude that a pigeonite-bearing residue is produced. Nevertheless, the abundances of low-Ca pyroxene that we calculate are in agreement with theirs.

The melting sequence derived from the analogous calculation in MAGPOX (Fig. 4b) appears at first glance to be dramatically different: according to MAGPOX, the initial ratio of augite to low-Ca pyroxene (lpyx) is much higher (thus plagioclase is eliminated before augite), and the low-

Ca pyroxene is always orthopyroxene (pigeonite does not appear in the melting sequence at all). However, this sequence implies a configuration of phase boundaries (Fig. 4b, right) that differs only slightly from that inferred from MELTS (Fig. 4a, right)—the main difference being that the orthopyroxene–pigeonite boundary is located at slightly higher *Wo*. Thus, this comparison reveals a slight discrepancy between the two programs with respect to the *mg* dependence of the orthopyroxene–pigeonite boundary, but nevertheless substantiates the conclusion that strictly chondritic precursor compositions will not produce ureilite-like residues, since in either program the case most likely to do so (the lowest *mg* of the ureilite range) does not.

Secondly, the suggestion (Kita et al., 2004) that fractional melting might allow pigeonite bearing ureilitic residues to be produced from chondritic precursors could be critical to our work. Unfortunately, fractional melting cannot be modelled with precision using MAGPOX, because the program does not calculate the compositions of low-degree melts (<3–4%) reliably. This is also the case with MELTS, which (as discussed by Kita et al., 2004) reports implausibly high SiO_2 and Na_2O contents. However, a qualitative analysis in the Opx–Plag–Wo system (Fig. 3) suffices to demonstrate that fractional melting of chondritic compositions is unlikely to lead to ureilite-like olivine–pigeonite residues. The earliest melts in this system must plot at the aug–lpyx–plag cosaturation point (“peritectic”)—the temperature minimum of the liquidus surface—and will remain there until one phase (either plagioclase or augite, for compositions relevant to this discussion) is exhausted. The location of this point varies slightly with *mg* and alkali content, but in all cases is close to the locus of chondritic Ca/Al ratio. For CM at *mg* 77 it is at slightly lower Ca/Al and slightly higher Plag than the bulk (nearly directly right of it), in the region of orthopyroxene stability (Fig. 3). Fractionation of early melts will therefore move residues along a path of nearly constant *Wo* (directly left), which does indeed pass through successively higher Ca/Al. This does not, however, necessarily imply that they will pass into the pigeonite field. In fact, it can be seen that the likelihood of this is low, as their path is nearly parallel to the orthopyroxene–pigeonite boundary. This argument is substantiated by the fractional melting simulation that Kita et al. (2004) performed for this composition (using MELTS, with 5% melt increments). The compositions of their residues (black stars in Fig. 3) increase in Ca/Al by a factor of >3 in the course of 23% melting; yet only the final residue reaches the pigeonite field and it contains only ~4% pigeonite, far too little to match an olivine–pigeonite ureilite of *mg* ~77 (Fig. 2).

This analysis supports the conclusion that starting compositions with superchondritic Ca/Al are required to produce ureilite-like residues, and indicates that this is the case even if melt extraction was fractional. The required Ca/Al ratios have been reevaluated, however. Higher values are needed to produce pigeonite-bearing residues at higher *mg*, and the analysis of Goodrich (1999) was constrained to match the most magnesian ureilite (Fo 94). However, it is now recognized that all ureilites of $Fo \geq 87$ are either orthopyroxene-bearing residues (Table 1, Fig. 2) or augite-bearing

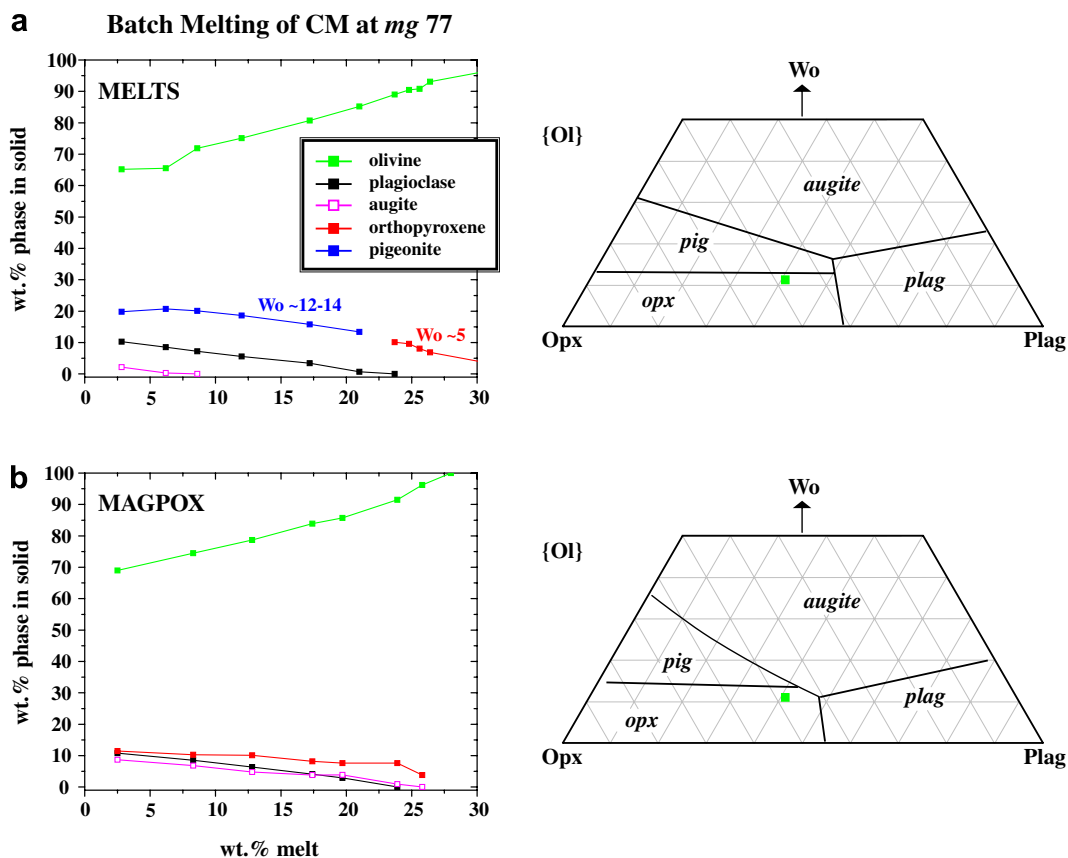


Fig. 4. Comparison between batch melting sequence of bulk CM reduced to *mg* 77 calculated (a) using MELTS ($fO_2 = IW - 1.5$, $P = 125$ bars) and (b) using MAGPOX. Phase diagrams for Opx–Plag–Wo system (projected from OI) illustrate that the two programs differ slightly on the location of the orthopyroxene/pigeonite boundary as a function of *mg* (boundaries in [a] inferred from the compositions of melts and calculated melting sequence; boundaries in [b] calculated with MAGPOX for the point of augite exhaustion). Despite this discrepancy, both programs indicate that batch melting of CM at *mg* 77 (~ the most ferroan of the ureilite *mg* range) produces an olivine–orthopyroxene, rather than a ureilite-like olivine–pigeonite, residue. Since at higher *mg* (e.g. the rest of the ureilite range), the stability of orthopyroxene relative to pigeonite increases, it is clear that no ureilites can be simple residues from batch melting of CM.

ing cumulates (Goodrich et al., 2004, 2006). The highest Ca/Al ratio now required is only $\sim 2.5 \times CI$.

The requirement for various non-chondritic Al/Mg ratios in ureilite precursor materials (Goodrich, 1999) arose from the fact that the ureilite data available at the time did not show the correlation between pyroxene/olivine ratio and Fo that would be a consequence of various degrees of smelting of a homogeneous composition. This requirement can now be eliminated, as new data (Fig. 2) do show the expected correlation. Using a composition with Ca/Al = $2.5 \times CI$ and Al/Mg = CI, a reasonable match to the ureilite data can be obtained over the full range of *mg*.

The requirement for an OC-like Si/Mg ratio in ureilite precursor materials (Goodrich, 1999) seems unsatisfactory from a theoretical point of view, as all other indications are that the parent body was CC-like. This higher value (relative to CC) was used to increase pyroxene/olivine ratios at all *mg* to match those of ureilites. However, our comparison between MAGPOX and MELTS suggests that this may not be necessary. For example, our bulk composition with Ca/Al = $2.5 \times CI$ at *mg* 76 produces (at the point of augite exhaustion) an olivine–pigeonite residue with

~ 26 vol% pigeonite in MAGPOX but $\sim 45\%$ in MELTS, a difference which greatly exceeds that due to the difference in the *mg* dependence of the orthopyroxene–pigeonite boundary (as noted above, MELTS calculates a higher ratio of low-Ca pyroxene to augite). Thus, if we were using MELTS it would be necessary to lower the Si/Mg ratio of the starting material to a CC-like value in order to produce ureilites. The source of this discrepancy between MAGPOX and MELTS appears, at least in part, to be due to a difference in distribution of Wo between augite and pigeonite, and new experimental data may be required to fully resolve it. For the present, we must retain the OC-like Si/Mg ratio, but note that it is likely artificial (i.e. a substitute for the proper correction to MAGPOX).

Finally, we have also considered the conclusion of Kita et al. (2004), based on modelling of feldspathic clasts in polymict ureilites, that ureilite precursor materials must have been alkali-undepleted. Our results remain at odds with this conclusion, as all calculations we have made using alkali contents higher than those (low CV) used by Goodrich (1999) fail to produce ureilite-like residues (principally because alkalis increase the stability of orthopyroxene

Table 2
Model ureilite precursor material at various degrees of reduction

Wt%	<i>mg</i> 62.3	<i>mg</i> 76	<i>mg</i> 91
SiO ₂	40.3	46.2	52.0
TiO ₂	0.13	0.15	0.17
Al ₂ O ₃	2.29	2.62	2.96
Cr ₂ O ₃	0.56	0.65	0.73
FeO	26.8	16.1	5.6
MgO	24.8	28.5	32.1
MnO	0.29	0.31	0.31
CaO	4.55	5.22	5.88
K ₂ O	0.03	0.04	0.04
Na ₂ O	0.20	0.20	0.22
Fe/Mg ^a	0.61	0.32	0.098
Fe/Mn ^a	91.1	51.3	18.4
Al/Mg/CI	1	1	1
Ca/Al/CI	2.5	2.5	2.5
Si/Mg/CI	1.08	1.08	1.08
K/Mg/CI	0.28	0.28	0.28
Na/Mg/CI	0.07	0.07	0.07

^a Molar values.

relative to pigeonite). However, we note that the petrogenesis of feldspathic clasts in polymict ureilites is poorly understood (Cohen et al., 2004; Kita et al., 2004). For example, Kita et al. (2004) assume that they are direct products of UPB melts. They may instead represent melts that have evolved through fractional crystallization (Goodrich et al., 2004), which would have increased their alkali contents. Thus, it is not clear that the calculations of Kita et al. (2004) provide a robust constraint on the composition of ureilite precursor materials.

In summary, the composition for ureilite precursor materials that we use in this work (Table 2) is CV-like (and assumed to have a bulk Fe content similar to that of Allende), except for having Ca/Al $\sim 2.5 \times$ CI. It is unlikely that this superchondritic Ca/Al ratio was a primary feature of the UPB (Goodrich, 1999). Goodrich et al. (2002) suggested that Ca was mobilized and concentrated during pre-igneous aqueous alteration (which is probably an inevitable consequence of heating a carbonaceous chondrite asteroid: Cohen and Coker, 2000), as evidenced in dark inclusions in CV chondrites with Ca/Al ratios up to $\sim 4 \times$ CI (Frusland et al., 1978; Bischoff et al., 1988; Johnson et al., 1990; Krot et al., 1995, 1997, 1998). This idea remains to be tested, but the bottom line for this work is that without superchondritic Ca/Al ratios we cannot model melting on the UPB, as ureilite-like residues will not be produced.

3. MELTING AND SMELTING ON THE UPB

3.1. Simultaneous melting and smelting at various pressures

A number of studies have discussed carbon redox control (regardless of whether they used the term smelting) on the UPB (Berkley and Jones, 1982; Warren and Kallemeyn, 1992; Goodrich et al., 1987; Walker and Grove, 1993; Sinha et al., 1997; Singletary and Grove, 2003, 2006). These studies focussed on estimating pressures of equilibration, from either thermodynamic or experimental

constraints, based on the assumption that carbon redox equilibrium was attained for the final, high-temperature assemblages now represented by the olivine–pigeonite ureilites. No studies so far have examined the *progress* of the smelting reaction during the course of melting, which could be critical if melting were a fractional, rather than batch, process. Here we do so.

Fig. 5 shows the location of our model ureilite precursor material (Table 2) in the Opx–Plag–Wo system at various degrees of reduction/smelting (we assume that its superchondritic Ca/Al ratio was already established by the time the silicate solidus was reached). At *mg* ~ 62 (no smelting) it plots in the augite field (suggesting that at greater depths on the UPB than those represented by known ureilites, ureilitic residues should contain augite as their sole pyroxene). Progressive smelting moves it directly toward Opx: at *mg* ~ 66 , it enters the pigeonite field, and at *mg* ~ 87 it enters the orthopyroxene field (phase boundaries are those corresponding to the point at which augite is exhausted in the melting sequence). Fig. 6a–d shows corresponding batch melting sequences calculated (with MAGPOX) for this composition at *mg* ~ 76 (\sim the low end of the ureilite range), 83, 87 and 91 (\sim the high end of the range for olivine + low-Ca pyroxene ureilites), respectively, and illustrate the change in mineralogy of the final residue (at \sim the point of augite exhaustion: Goodrich, 1999; Singletary and Grove, 2003) with increasing degrees of smelting: in particular, pyroxene/olivine ratio increases, and at higher *mg* orthopyroxene appears and begins to replace pigeonite. For each *mg*, the accompanying Opx–Plag–Wo diagram show the location of phase boundaries at the solidus and at the point of augite exhaustion, and illustrates the path of the liquid during melting. At low *mg* (~ 66 –86), the orthopyroxene–pigeonite boundary is below the peritectic point (i.e. the peritectic point is within the pigeonite field), and the only pyroxene present throughout the melting sequence is

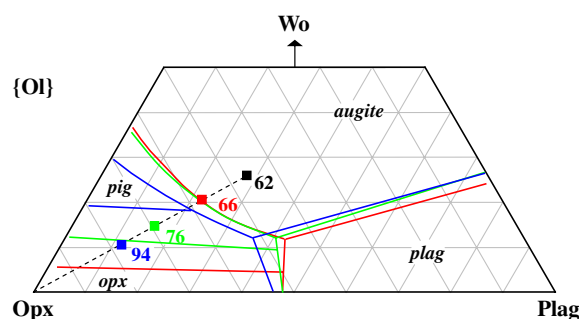


Fig. 5. Opx–Plag–Wo system showing model ureilite precursor material used in this study (Ca/Al = $2.5 \times$ CI) at various degrees of reduction (in various colors, labelled *mg* 62–94). Bulk UPB is assumed to have a total iron content similar to that of Allende (*mg* ~ 62 , if all iron occurs as FeO), and plots in the augite field; thus, unsmelted UPB residues (at depths corresponding to pressures greater than ~ 100 –125 bars; see Fig. 1) should contain augite as their sole pyroxene. This composition produces olivine–pigeonite residues at *mg* ~ 66 –86 and olivine–orthopyroxene–(pigeonite) residues at *mg* ≥ 87 (after augite is exhausted). Phase boundaries shown (in same colors as the corresponding bulk compositions) are for approximately the point of augite exhaustion.

pigeonite. At $mg > \sim 87$, the orthopyroxene–pigeonite boundary is above the solidus (i.e. the peritectic point is within the orthopyroxene field), and the only pyroxene present at the beginning of the melting sequence is orthopyroxene. As melting proceeds, however, the liquid overtakes the orthopyroxene–pigeonite boundary, and pigeonite begins to form at the expense of orthopyroxene. Pigeonite/orthopyroxene increases until augite is exhausted (and their ratio at this point decreases with increasing mg), at which point the trend reverses and orthopyroxene begins to dominate (actually, for all $mg > \sim 83$, the bulk composition is within the orthopyroxene field and so at very high degrees of melting olivine–orthopyroxene residues are produced). Finally, at higher mg than illustrated (i.e. mg 94), the orthopyroxene–pigeonite boundary is located at sufficiently high Wo that the melt never overtakes it, and the only pyroxene ever present is orthopyroxene. It is important to note that our model does not explicitly involve the olivine \rightarrow low-Ca pyroxene reaction boundary in the olivine–quartz–wollastonite (Ol–Qtz–Wo) system, because we assume that ureilites are produced as residues at the point of augite exhaustion.

By comparison to Fig. 2, it is clear that the melting behavior of this composition over a range of increasing mg , as predicted by MAGPOX, can lead to the observed trend of pyroxene/olivine ratio and pyroxene types seen in ureilites. However, the exact calibration of MAGPOX (i.e. the location of the orthopyroxene–pigeonite boundary as a function of mg) relative to available experimental data, remains uncertain. For example, the calibration used for the calculations shown in Fig. 6 locates the orthopyroxene–pigeonite boundary at slightly lower temperature (by $\sim 20^\circ$), for a given mg , than the data of Grove and Juster (1989). This produces a good match to the mg (~ 87) at which orthopyroxene appears in the ureilite data, whereas a more exact calibration to the experimental data would shift this point to $mg \sim 83$ and result in complete loss of pigeonite for $mg > \sim 87$ (inconsistent with what is seen in ureilites). This slight mismatch, however, should not be considered fatal, as the dependence of the orthopyroxene–pigeonite boundary on mg is likely sensitive to a variety of factors that are not completely understood.

Although each of the melting sequences shown in Fig. 6a–d might be thought to correspond to a particular

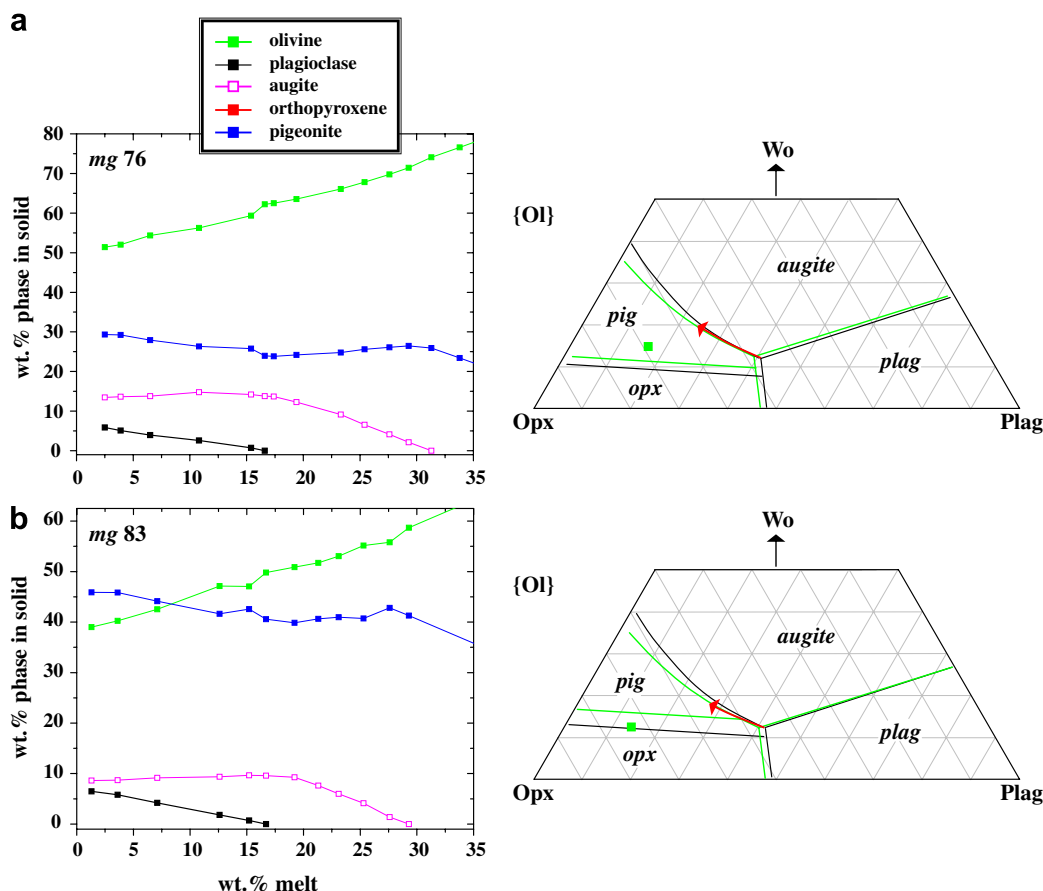


Fig. 6. Results of calculations with MAGPOX showing batch melting sequences for model ureilite precursor material ($Ca/Al = 2.5 \times CI$) at increasing mg (increasing degrees of smelting, decreasing depth). Ureilite-like residues (appropriate olivine/pyroxene ratios and pyroxene types) are produced in the range $mg \sim 76$ –91 (results from these calculations are converted to vol % and compared to the ureilite data in Fig. 2) at $\sim 30\%$ melting, just after complete removal of augite. Accompanying diagrams for the Opx–Plag–Wo system (projected from Ol) illustrate location of phase boundaries at the solidus (black lines) and at the point of augite exhaustion (green lines), for each mg . Red arrows show path of melt composition, ending at the point of augite exhaustion. Green squares represent bulk compositions. These compositions can be considered to be “pre-smelted” in the sense that the melting sequences do not take into consideration the course of smelting during melting.

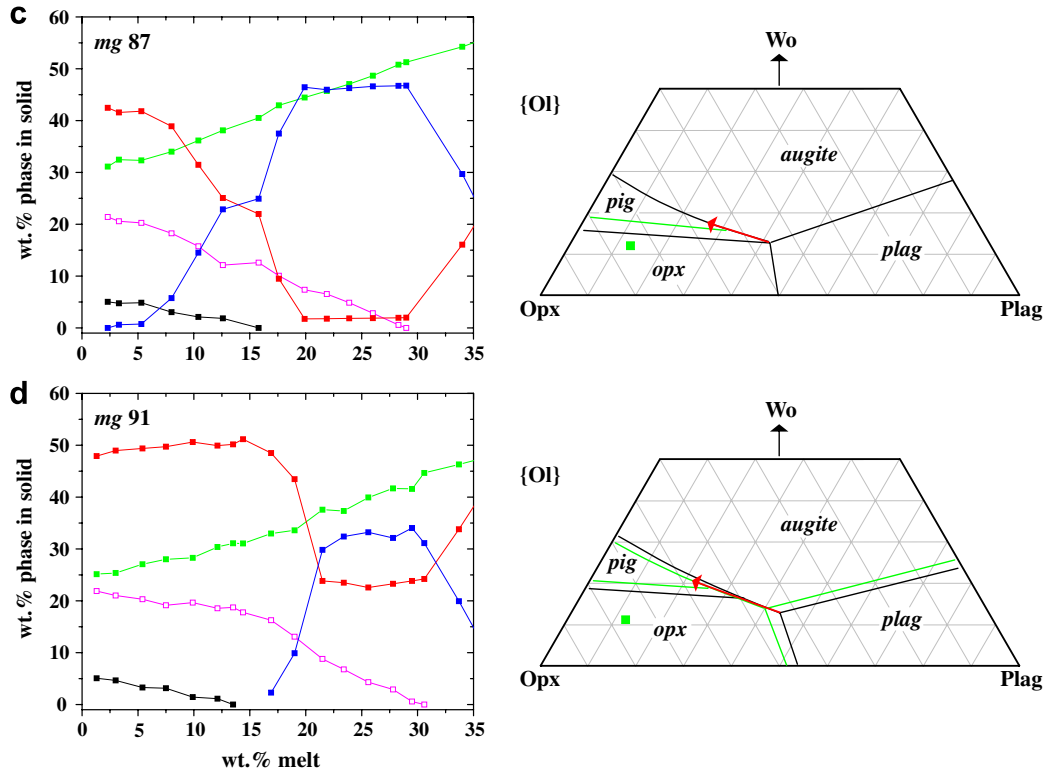


Fig. 6 (continued)

depth (pressure) on the UPB, this view is misleading because in each case the starting composition (source region) was assumed to have already had the appropriate FeO content to produce a final residue of a certain *mg*; i.e. it was assumed to be “pre-smelted.” In fact, our model assumes that the UPB was originally homogeneous in FeO content (with *mg* ~62, as in Allende), and that in each source region (depth), the mineralogy of the residue evolved in response to progressive smelting as well as progressive melting.

Consider first a source region located at a depth equivalent to ~30 bars pressure (the pressure of equilibration of the most magnesian ureilite, based on the thermodynamic treatment in Fig. 1). Smelting begins at ~1060 °C, the temperature at which carbon redox reactions buffer an *mg* value near that of the bulk UPB (~62); at this point, the carbon redox system is in equilibrium and gas pressure is assumed to be equal to total lithostatic pressure. This is also the approximate solidus temperature for this composition (from MAGPOX, with an uncertainty of ± 20 °C), and so smelting and melting begin simultaneously (Fig. 1). In contrast, for a source region located at a depth equivalent to ~100 bars pressure (the pressure of equilibration of the most ferroan ureilite), smelting does not begin until *T* has reached just over 1200 °C, where the 100 bar graphite–gas curve intersects the olivine–silica–metal buffer for *mg* ~62 (Fig. 1). For source regions located at intermediate depths (pressures), smelting begins at temperatures between 1060 and 1200 °C (e.g. ~1140 °C at 65 bars). In all cases, as temperature continues to increase, carbon redox equilibria buffer progressively higher *mg* values (i.e., the graphite–gas

curves cross olivine–silica–metal curves of progressively higher *mg*), and smelting proceeds further. The relationships between *mg* and *T*, for each of 30, 65 and 100 bars pressure, are shown in Fig. 7a.

In order to determine the mineralogical evolution of ureilitic residues in response to simultaneous melting and smelting, we first determined wt% melt vs. *T* functions for individual pre-smelted compositions in the range *mg* 76–94 and combined them, using the relationships between *T* and *mg* (Fig. 7a), to produce actual (simultaneous smelting) wt% melt vs. *T* functions for 30, 65, and 100 bars pressure (Fig. 7b). We then combined the relationships in Fig. 7a and b, for each of the three pressures, to produce wt% melt vs. *mg* functions (Fig. 7c). Finally, guided by these functions, we used MAGPOX in a series of incremental calculations (altering the *mg* of the starting composition for each melting interval) to simulate simultaneous melting and smelting. The resulting melting sequence for each pressure (both the mineralogical evolution of the residue and the path of progressive melts in Opx–Plag–Wo) are shown in Fig. 8.

At 100 bars (Fig. 8a), smelting does not begin until ~21% melting, and so up until this point the melting sequence is identical to that of the *mg* 62 starting material; pigeonite is not present, and augite is the only pyroxene. Pigeonite appears when smelting begins, and increases steadily in abundance as augite is progressively lost. The final olivine–pyroxene residue (Fo ~ 76) at the point of augite exhaustion contains ~26 wt% pigeonite, which is a good match to the ureilite data (Fig. 2). Note that this sequence

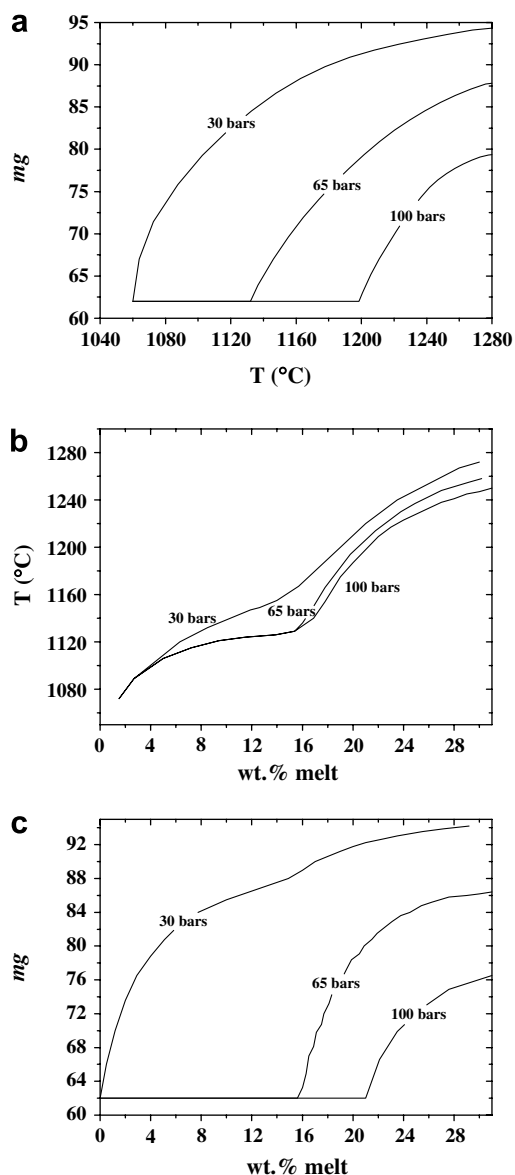


Fig. 7. (a) Temperature vs. *mg* (Fo of olivine) buffered by smelting at 30, 65, and 100 bars pressure (encompassing the range of equilibration pressures estimated for ureilites). These relationships were determined by simultaneous (graphical) solution of the graphite–CO + CO₂ equilibria and the olivine–silica–metal equilibria shown in Fig. 1. (b) Wt% melt vs. *T* for simultaneous melting and smelting at 30, 65, and 100 bars pressure on the UPB. These relationships were determined by combining individual wt% melt vs. *T* functions for constant *mg* (pre-smelted compositions, as in Fig. 6), using the relationship between *T* and *mg* shown in (a). (c) Wt% melt vs. *mg* for 30, 65, and 100 bars pressure on the UPB. These relationships were determined by combining the relationships in (a) and (b), for each pressure.

(both the mineralogical evolution of the residue and the compositions of progressive melts) differs considerably from the pre-smelted *mg* 76 sequence (Fig. 6a). At 65 bars (Fig. 8b), the melting sequence is similar, except that smelting begins and pigeonite appears earlier (at ~16% melting) and the final residue (Fo ~ 86) contains ~46 wt% pigeonite

(also a good match to the ureilite data). Again, this sequence differs considerably from that of a pre-smelted *mg* 86 composition. At lower pressures, the mineralogical evolution of the residue is more complex, because of the appearance of orthopyroxene at *mg* >~86. At 30 bars (Fig. 8c), where melting and smelting begin nearly simultaneously, pigeonite is present initially and increases in abundance with progressive smelting during melting. However, at ~11% melting, *mg* has reached ~86 and orthopyroxene appears. Orthopyroxene now increases at the expense of pigeonite until *mg* reaches ~91; here, the composition of the melt passes the orthopyroxene–pigeonite–augite cosaturation point and the orthopyroxene/pigeonite trends reverse (the resurgence of pigeonite here is the same effect as observed in the pre-smelted compositions of *mg* ≥87, but it is tempered by the increase of orthopyroxene due to progressive smelting).

3.2. CO + CO₂ gas production during melting

The results of our calculations for simultaneous melting and smelting at various pressures (Fig. 8) have significant implications for the generation of CO + CO₂ gas, particularly in the case of fractional melting. Although previous workers (Warren and Kallemeyn, 1992; Scott et al., 1993; Warren and Huber, 2006) have estimated the amount of CO + CO₂ gas generated by smelting on the UPB (in the interest of evaluating explosive volcanism), none of them considered the progress of gas production during the course of melting. From Fig. 8, it is clear that gas production will vary significantly during the course of melting; furthermore, it will vary with depth. The relationships between degree of melting and *mg* shown in Fig. 7c allow us to calculate the amounts of CO + CO₂ gas generated as a function of melting at each depth (pressure) in the UPB. We have assigned the starting material a uniform carbon content (5 wt%) sufficient to guarantee smelting up to at least *mg* ~94 (though it may have been higher and not necessarily homogeneous), and utilize the stoichiometry of the simplest reduction reactions (reduction of 1 mole of FeO yields 1 mole of CO or 0.5 moles of CO₂). Total gas pressure is assumed to be equal to lithostatic pressure, and the ratio between CO and CO₂ (as a function of *T* and *P*) is obtained from the formulations of French and Eugster (1965). Results are shown in Fig. 9.

Consider first the shallowest source regions (30 bars pressure), where gas production begins at approximately the same time as melting. Assuming a batch melting process, nearly 10 wt% gas (of which 90–100% is CO) has been produced by the time silicate melting ends (~29% melt), implying a concentration of ~31% gas in the melt (or ~23% in the total melt + gas fluid phase). However, if melting is a fractional process, we need to consider the gas contents of small increments of melt. Because the rate of smelting (relative to melting) is initially high, the ratio of gas to melt in the system will be very high in the earliest stages of melting. This ratio rapidly decreases as melting and smelting proceed. This is shown quantitatively in Fig. 10, where we plot the amount (wt%) of gas generated during each 1% melting interval (gas/melt ratio by mass).

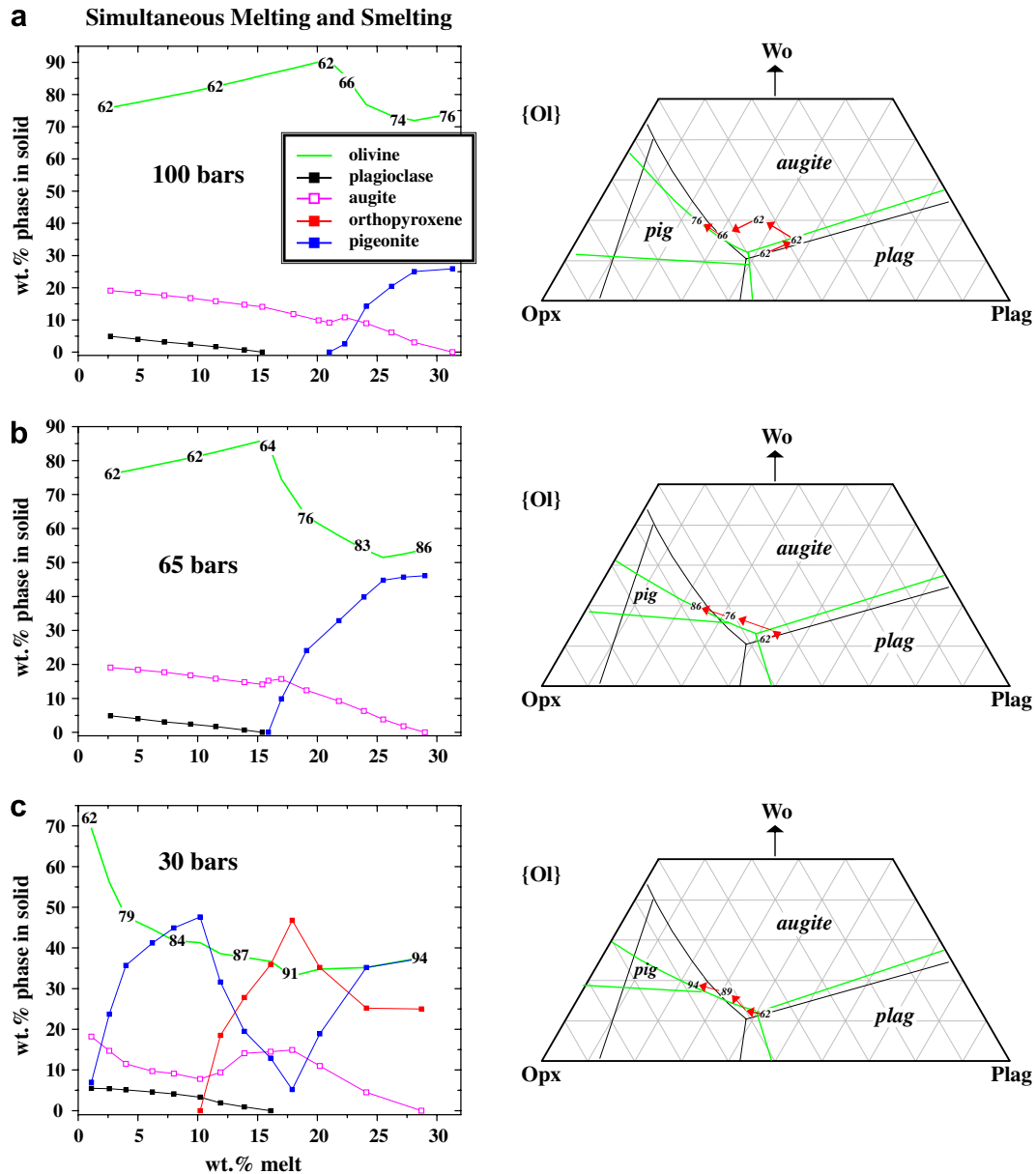


Fig. 8. Calculated sequences for simultaneous melting and smelting at 30, 65 and 100 bars pressure on the UPB, determined by combining results of individual MAGPOX calculations for constant mg (pre-smelted compositions, as in Fig. 6), using the relationship between degree of melting and mg shown in Fig. 8c. Values of mg are superimposed on the olivine curves. Note that these melting sequences differ considerably from the sequences for pre-smelted compositions shown in Fig. 6. Accompanying diagrams for the Opx–Plag–Wo system (projected from Ol) illustrate location of phase boundaries at the solidus (black lines) and at the point of augite exhaustion (green lines). Red arrows show path of melt composition, ending at the point of augite exhaustion. Selected melts indicated by mg values showing the progression of smelting.

In the initial few 1% increments, the ratio of gas to melt is >1 (as high as 2.5); in the final fifteen (\sim half of the total melting interval), it is ≤ 0.05 (Fig. 10).

In the deepest source regions (~ 100 bars pressure) smelting does not begin, and therefore no gas is generated, until $\sim 21\%$ melting has occurred. The total amount of gas generated by the time melting is complete is $\sim 5.3\%$, which would imply a concentration of $\sim 18\%$ in a batch ($\sim 29\%$) melt. In the case of fractional melting, the first 20 1% melt increments contain no gas (Fig. 10). The next increment, however, has a gas/melt ratio of ~ 1.7 . This rapidly declines,

so that in the final (3–4) steps of melting it is, as in the shallowest source regions, very low (≤ 0.05). Thus, the general picture is that the onset of smelting results in a burst of gas production and very high gas/melt ratios. In the shallowest source regions this occurs near the beginning of melting; in the deepest source regions it does not occur until near the middle of the melting sequence (and, notably, after plagioclase has been exhausted from the residues). In all source regions, however, these initially high values rapidly decline. Another point is that deeper source regions on the UPB (corresponding to pressures greater than ~ 125

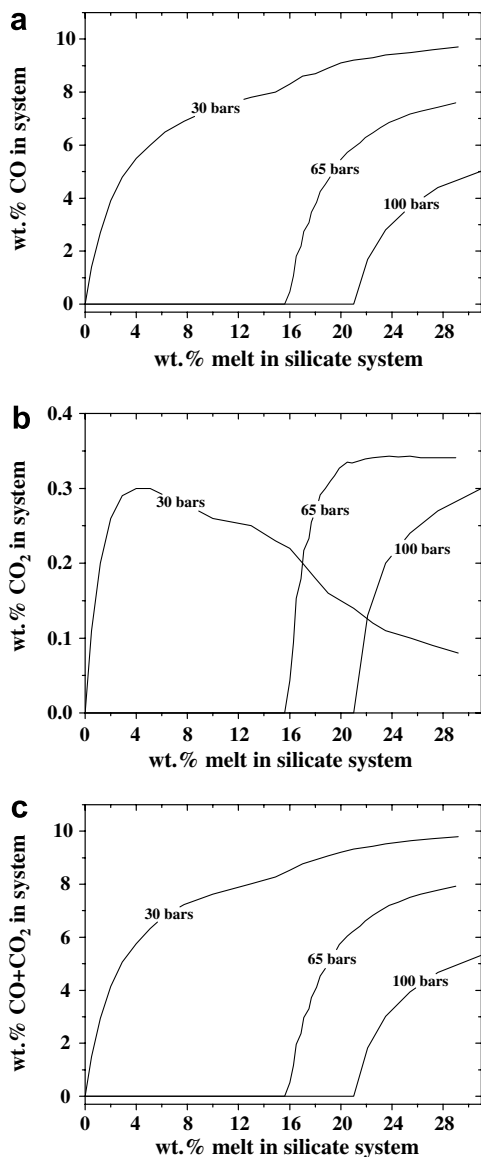


Fig. 9. Gas (CO and CO₂) production due to progressive smelting at 30, 65 and 100 bars pressure on the UPB. These functions were determined by combining the wt% melt vs. *mg* relationships in Fig. 7c with the basic smelting reaction. Ratio between CO and CO₂ (as a function of *T* and *P*) taken from the formulations of French and Eugster (1965).

bars) would not have produced any gas, since they did not experience smelting. (Fig. 1).

3.3. Effect of fractional melting on smelting

In the preceding discussion we considered the implications of fractional melt removal with respect to the concentration of gas in the melt. Paradoxically, however, one of the consequences of fractional melt removal is that the gas produced by smelting would be continuously removed from the system (in fact, it might be continuously removed from the system even in a batch melting situation, based on buoyancy), which implies that carbon redox equilibrium

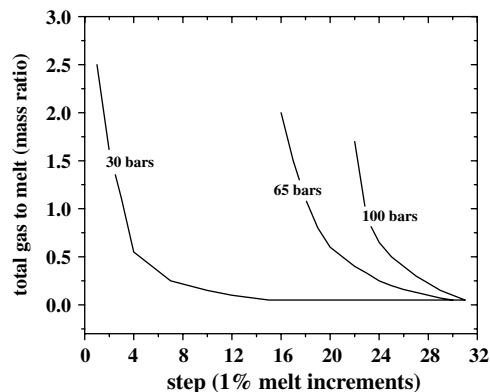


Fig. 10. Incremental production of gas (CO and CO₂) due to smelting during melting at 30, 65 and 100 bars pressure on the UPB.

would not be maintained. This situation was seen by Warren and Huber (2006) as a runaway (“gas-leaky”) process that could not produce the array of *mg* (Fo) seen in ureilites. However, their discussion neglected the fact that smelting is occurring during heating (Fig. 11). For a source region located at a depth equivalent to ~30 bars pressure, the system is in carbon redox equilibrium at ~1060 °C and Fo ~ 62. At this point, both melting and smelting begin. If the melt is instantaneously removed and takes the gas with it, the smelting reaction ($\text{FeO} + \text{C} \rightarrow \text{Fe} + \text{CO}$) must be driven to the right. This results in a drop in oxygen fugacity (down arrows) and the system is no longer in equilibrium. However, temperature is rising, and as it does so the system will return to equilibrium (diagonal arrows parallel to Fo curves). This process will be repeated in a series of infinitely small steps, until melting is complete (heating ends) and the final residue reaches Fo ~ 94; this residue will be at equilibrium provided the last tiny increments of melt and gas are not removed.

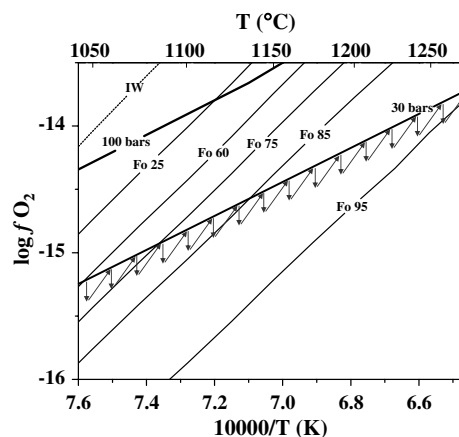


Fig. 11. Schematic illustration of incremental evolution of $f\text{O}_2$ (dark grey arrows) in $f\text{O}_2$ –*T* space during simultaneous fractional melting and smelting at constant pressure (depth).

3.4. Smelting of melts during ascent

One of the consequences of upward migration of melts on the UPB is that if they carry graphite with them (the low density of graphite would be conducive to this, but the grain size of graphite might preclude it being transported in initial melt conduits), they would be progressively smelted. Fig. 12 shows, for example, calculated contents of CO + CO₂ that would be generated by smelting during isothermal ascent of melts in the range 1050–1250 °C. These gas contents (up to ~11 wt%) are substantial, and would be an additional contribution (beyond gas generated by smelting in the source region) to explosive volcanism. However, if all melts were smelted in this way during ascent to the surface (or near-surface) of the UPB, they should all be highly magnesian. This prediction is in contrast to what is observed in polymict ureilites. Several of the indigenous feldspathic melt lithologies that have been identified (including the most abundant) in polymict ureilites are notably more ferroan than monomict ureilites (Ikeda et al., 2000; Cohen et al., 2004). Furthermore, the very fact that they were preserved (as opposed to being lost by explosive volcanism) might suggest that they did not contain excessive gas. Nevertheless, the exact relationship of these clasts to monomict ureilites is poorly understood, and their ferroan compositions might also be explained by late fractionation after complete consumption of carbon (Cohen et al., 2004). Thus, the question of whether melts on the UPB carried graphite with them during ascent remains open.

3.5. Effect of fractional melting on compositions of melts

The melting sequences shown in Fig. 8 incorporate the effect of progressive smelting during melting, but are still batch melting sequences. This approximation is necessary since, as noted above, fractional melting cannot be modelled precisely enough with MAGPOX. Nevertheless, we can determine the general effect of fractional melting on

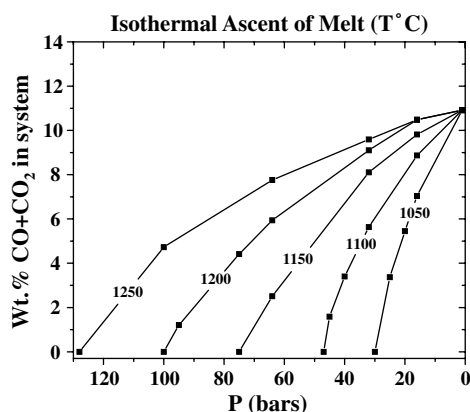


Fig. 12. Production of gas (CO and CO₂) by smelting as a function of pressure at various constant magmatic temperatures. Melts on the UPB may carry carbon with them as they migrate upwards. If so, they will experience progressive smelting due to decreasing pressure.

the compositions of melts and residues from a crude calculation. Fig. 13 shows (in the Opx–Plag–Wo system) the results of a fractional melting simulation for our model ureilite precursor material at *mg* 76 (cf. Fig. 6a). Melts were fractionated in 5% intervals, up to 30% total melting. Comparison of the fractional with the batch residues shows that the difference is not extreme (mainly due to lower Al₂O₃ contents in the fractional residues), and in fact might be difficult to detect in actual ureilites (though we do note that typical olivine–pigeonite ureilites have Al₂O₃ contents near ~0.25 wt% [Mittlefehldt et al., 1998], which is close to the prediction of the fractional calculation). In contrast, the difference in melt compositions is quite large: namely, fractional melts quickly develop Ca/Al ratios significantly higher than those of the batch melts. This result then, has implications that could be further examined by comparison to feldspathic materials in polymict ureilites.

We have not attempted to combine simultaneous melting and smelting with fractional melt removal because the compounding of errors from two relatively crude iterative calculations is likely to be so large that results would not be meaningful. Nevertheless, the effect should be similar to what is seen in Fig. 13, namely melt compositions may be significantly more refractory, but residues will be only minimally different from those in the batch melt/smelt calculations (Fig. 8).

3.6. Explosive volcanism

Our new estimates of CO + CO₂ gas production due to smelting remain consistent with the suggestion (Warren and Kallemeyn, 1992; Scott et al., 1993) that melts generated on the UPB were lost to space by explosive volcanism (Wilson and Keil, 1991). However, the recognition that in all but the shallowest source regions, some portion (in fact, more than half in the deepest) of the melting sequence occurred in the absence of smelting, implies that by no means were all melts thus lost. Our calculations (details to be published separately) indicate that the total of the smelted melts that would have erupted explosively corresponds to ~10% of

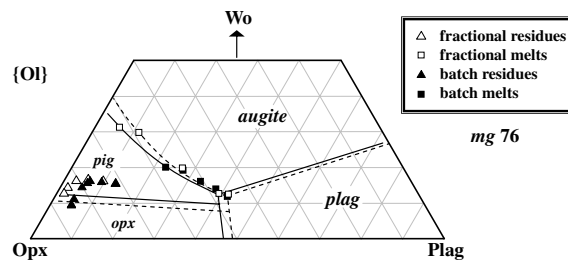


Fig. 13. Comparison of compositions of melts and residues from ~30% fractional vs. batch melting. Fractional melting simulated by an iterative calculation in 5% melt increments. Bulk composition (*mg* 76) is the same as in Fig. 6a. Although fractional residues differ only slightly from those of batch residues, fractional melts evolve to significantly higher Ca/Al ratios than batch melts. Dashed lines are phase boundaries at solidus; solid lines are phase boundaries at point of augite exhaustion (~30% melting).

the initial 100-km radius asteroid volume, while the total of non-smelted melts, which ultimately would have erupted non-explosively to form a crust, represents $\sim 8.8\%$. Warren and Huber (2006) argue that the loss of asteroid mass due to explosive volcanism would have led to a diminution in pressure that would have fed the runaway smelting process they envision (as discussed above). However, the loss of 10 vol % of a 100-km body corresponds to a reduction in its radius of only $\sim 3\%$ —from 100 km to ~ 96.5 km. While it is true that this change in radius has a proportional effect on the variation of pressure with depth, this occurs progressively during the melting process and is not large enough to have a significant effect on any of our calculations. Furthermore, although it has been proposed that the UPB never had any crust, our calculations suggest that it may have had thin crust, encompassing the outer ~ 3.3 km of the final body.

4. PHYSICS OF MELT EXTRACTION ON THE UPB

The relationships derived above (specifically the melt/smelt sequences in Fig. 8 and the gas production curves in Fig. 9) provide essential input for modelling the physics (mode and rate) of melt extraction on the UPB. This work will be published separately, but results (presented in preliminary form in Wilson et al., 2006) are summarized here. Our calculations indicate that melts would have begun to migrate from their source regions (principally upwards under buoyancy forces) after only ~ 1 – 2% melting. Thereafter, they would have migrated continuously in a network of thin veins, coalescing upwards into fatter veins, and eventually into dikes. Full vein inter-connectivity would have been established very quickly, and thereafter the melt content of the vein network at any time would have been at most only $\sim 0.3\%$. Furthermore, melt migration rates would have been high, with the most conservative estimate of the time required for a given parcel of melt to pass through the system to the surface being in the range of 2 months to one year. Such rapid, continuous melt extraction, and migration in veins and dikes (as opposed to slow percolation along

grain boundaries) would have been conducive to preservation of oxygen isotopic heterogeneity in the mantle, since the distance that oxygen can diffuse in olivine in a year at 1200–1250 °C is on the order of only $1 \mu\text{m}$ ($D = 10^{-20} \text{ m}^2/\text{s}$; Dohmen et al., 2002).

5. TRACE ELEMENT FRACTIONATION DURING MELT EXTRACTION ON THE UPB

From the point of view of geochemical modelling, the process suggested by our physics calculations (Wilson et al., 2006) is perfect fractional melting, in which each infinitesimal batch of melt is removed instantaneously from its source region. This result can be tested further using trace elements such as rare earth elements (REE), which provide a sensitive indicator of batch vs. fractional melting. Warren and Kallemeyn (1992) modelled REE of ureilites, and concluded that they are not consistent with fractional melting. Here, we reevaluate this conclusion.

5.1. REE patterns of ureilites

Bulk REE data are available for 20 ureilites (Goodrich et al., 2004), but only eight of these are olivine + low-Ca pyroxene ureilites (i.e. residues relevant to our modelling) of low shock state (Fig. 14a). All of them show a V-shaped REE pattern, which is known to result from the presence of a cryptic, volumetrically minor LREE-enriched component that can be removed by leaching (Fig. 14b). The origin of this component is uncertain, but it is generally agreed to be secondary (Goodrich and Lugmair, 1995; Goodrich et al., 1995; Torigoye-Kita et al., 1995a,b) and not representative of the residual mantle composition. Therefore, only HREE will be used in our modelling.

Six of the patterns in Fig. 14a, all of which belong to olivine–pigeonite ureilites of low to intermediate *mg* (Fo ~ 78 – 83), show very similar HREE abundances. Of these, Kenna is the best studied. Two sets of leaching experiments have been performed on Kenna (Boynton et al., 1976; Spitz and Boynton, 1991). In the leached samples,

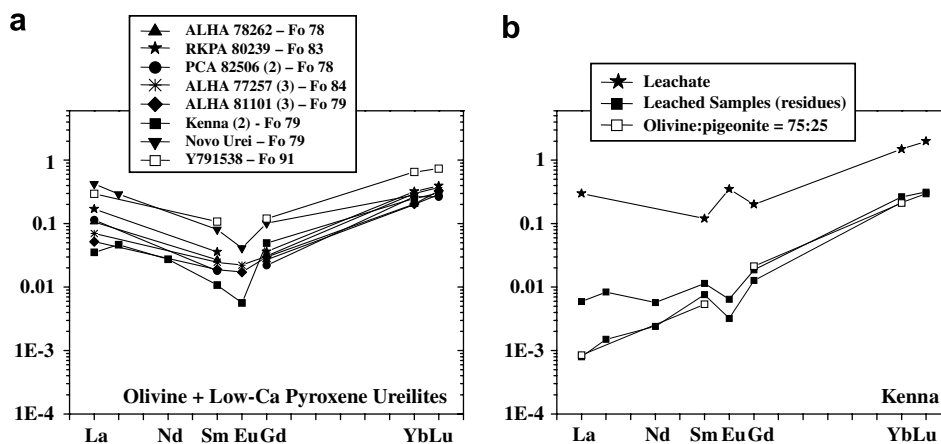


Fig. 14. REE for olivine + low-Ca pyroxene ureilites. Sources of data: Boynton et al. (1976), Guan and Crozaz (2000), Kallemeyn and Warren (1994), Spitz and Boynton (1991), Warren and Kallemeyn (1992).

HREE abundances are slightly lower and show a slightly steeper pattern than in bulk rock analyses; LREE are highly depleted, and show slightly lower abundances in one sample than in the other (Fig. 14b). REE have also been measured in situ (by SIMS) for Kenna olivine and pigeonite (Guan and Crozaz, 2000). A bulk REE pattern reconstructed from these data in modal proportions (olivine:pigeonite = 75:25) is essentially identical in HREE to the patterns of the leached whole-rock samples, and also essentially identical in LREE to the pattern of the leached sample with the lower abundances (Fig. 14b). Furthermore, Nd isotopic data indicate that material free of the LREE-enriched component should have a $^{147}\text{Sm}/^{144}\text{Nd}$ ratio of ~ 0.51 (Goodrich and Lugmair, 1995). This translates into an Sm/Nd ratio (~ 2.6) only slightly higher than that of the reconstructed pattern (~ 2.4). Thus, the REE pattern of one leached Kenna sample, and the pattern reconstructed from the individual Kenna minerals, appear to be the best data available to represent the residual mantle of the UPB. Kenna has Fo ~ 79 , and thus (in the smelting model) represents one of the deeper of the source regions that have been sampled. Only one REE pattern is available for an olivine–orthopyroxene ureilite representing shallow source regions (Y791538, Fo ~ 91). Its HREE abundances are slightly higher than those in the olivine–pigeonite samples, but we cannot be certain that this is significant. Therefore, in this work we limit our modelling to Kenna.

5.2. Starting material and melting sequence

In their REE modelling, Warren and Kallemeyn (1992) used a starting material containing 11.5% plagioclase (similar to unaltered CV chondrites), with olivine, pigeonite and augite in the ratio 75:20:5. They assumed that the phases being melted were half plagioclase and half mafic minerals, the latter in modal proportions. Plagioclase is eliminated at 23% melting, leaving a final residue consisting of 75% olivine, 20% pigeonite, and 5% augite. The conditions we use in our modelling differ from these in several respects.

First, in our interpretation only the olivine + low-Ca pyroxene ureilites are residues; therefore, the final residue should not contain augite. Second, we specify the bulk chemical composition of the starting material to be the model ureilite precursor composition discussed above (Table 2), and focus on modelling a Kenna-like residue—i.e. a source region at ~ 100 bars. The starting mineralogy is, therefore, ~ 76 wt% olivine, 19 wt% augite, and 5 wt% plagioclase (Fig. 8a). As melting proceeds before smelting, plagioclase and augite both decrease, and plagioclase is exhausted at $\sim 15\%$ melting. When smelting begins, at $\sim 21\%$ melting, pigeonite appears, and thereafter increases in abundance. Augite is exhausted at $\sim 33\%$ melting, leaving a Kenna-like olivine–pigeonite residue with ~ 26 wt% pigeonite (Fig. 2).

5.3. REE distribution coefficients

Experimentally determined REE crystal/liquid distribution coefficients for olivine, plagioclase, pigeonite and augite are reviewed by Jones (1995). Data most appropriate

for this work are summarized in Fig. 15. Values for plagioclase are those recommended for lunar basalts at ~ 1240 °C. Those for olivine are given by $\log_{10} D = -4.566 + 0.219 \times \text{REE}\#$ (though this parameterization likely gives Ce and Nd values that are too high: Jones, 1995). Pyroxene distribution coefficients are parameterized by Jones (1995) in terms of crystal/liquid distribution coefficients for Ca (D_{Ca}): $\log_{10} D = A \log_{10} D_{\text{Ca}} + B$. Regression parameters (A, B) for pigeonite and augite are given in Table 6 and “hypothetical” values for D_{Ca} for various meteoritic and terrestrial rock types are given in Table 7 of his paper. Of these, lunar mare basalts provide the most appropriate analog to ureilites, because lunar mare basalts represent liquids with superchondritic Ca/Al ratios (in contrast to eucrites which have \sim chondritic Ca/Al). Unfortunately, however, the lunar basalt D_{Ca} values for pigeonite and augite given by Jones (1995) are substantially different from those given for all other rock types (note too that they are not consistent with values determined by Grove and Bence, 1977) and are probably erroneous (Jones, personal communica-

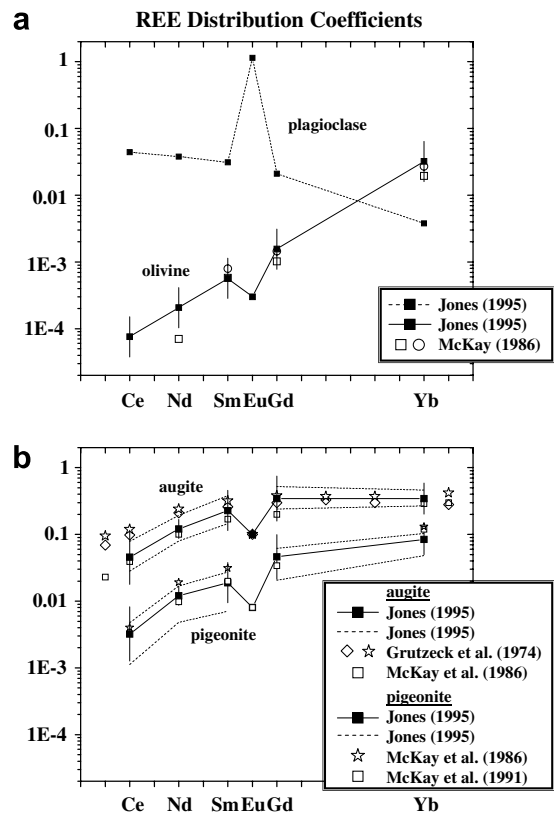


Fig. 15. REE distribution coefficients (D). (a) Values for plagioclase based on lunar basalts at 1240 °C (Jones, 1995). Values for olivine from Jones (1995) parameterized as $\log_{10} D = -4.56 + 0.219 \times \text{REE}\#$. Values for olivine from McKay (1986) are based on two types of lunar basalts. (b) Values for both pyroxenes from Jones (1995) parameterized in terms of “eucritic” D_{Ca} (solid lines), and also 1125 °C (upper set of dashed lines) and 1250 °C (lower set of dashed lines) values of D_{Ca} from Grove and Bence (1977). Values for augite from Grutzeck et al. (1974) correspond to $f\text{O}_2 = \text{IW} - 1$. Values for augite from McKay et al. (1986) are based on shergottites.

tion). Parameterization in terms of D_{Ca} also introduces a complexity in that D_{Ca} values are T -dependent. Fig. 15b shows the ranges of REE distribution coefficients for pigeonite and augite calculated from the parameterization of Jones (1995) using D_{Ca} values from Grove and Bence (1977) for 1125 and 1250 °C (\sim the T range over which melting occurs for our starting composition). These are similar to the total ranges of values measured in the most reliable experimental studies (Grutzeck et al., 1974; McKay et al., 1986). The D_{Ca} values suggested by Jones for eucrites correspond to a T of \sim 1175 °C (\sim an average T for our melting interval) when compared to the Grove and Bence (1977) data, and produce sets of REE distribution coefficients roughly in the middle of these ranges. In addition, the associated uncertainties (calculated from the 2-sigma values in Table 6 of Jones, 1995) correspond well to the total ranges. Therefore, for our nominal “best” set of values, we use those calculated from eucritic D_{Ca} .

The Eu distribution coefficients shown in Fig. 15 correspond to an oxygen fugacity (fO_2) of \sim 1W/10, which is appropriate for modelling Kenna. The plagioclase value is that cited by Jones (1995) for lunar conditions ($fO_2 < 1W$). The augite value is extrapolated to 1W/10 from the data of Grutzeck et al. (1974), and the pigeonite value is from McKay et al. (1991) for pigeonite of Wo \sim 8 at 1W/10. Olivine distribution coefficients are likely to have a substantial negative Eu anomaly at low fO_2 (Jones, 1995), but its magnitude (Fig. 15) is only a guess.

5.4. Modelling and results

We modelled incremental batch melting (Allegre and Minster, 1978) using a FORTRAN program (which we wrote ourselves) in which we could input any melting sequence to describe the evolution of the residual mineralogy. We used various selections of distribution coefficients within the ranges of uncertainty shown in Fig. 15, and for each selection calculated the REE pattern of the final residue (C_R/C_0 , where C_0 is assumed chondritic) for n (# of equal-sized steps of melt extraction) up to 75.

Fig. 16 compares the result obtained for the 100 bar simultaneous melting plus smelting sequence with that obtained from the melting sequence of Warren and Kallemeyn (1992), using the “best” values of all distribution coefficients (solid squares in Fig. 15). The latter is very similar (though not identical, probably because the distribution coefficients used are not quite the same) to that reported by Warren and Kallemeyn (1992) themselves. The $n = 1$ pattern (batch melting) for our melt/smelt sequence shows lower REE abundances and a steeper slope than that for the Warren and Kallemeyn (1992) sequence, because of the lack of augite in the residue. However, results for all higher values of n (larger number of extraction steps) show higher abundances and shallower slopes, due to the presence of larger amounts of augite in the residue throughout the melting sequence. Furthermore, our melting sequence produces negative Eu anomalies in the residues for all values of n (consistent with the negative Eu anomalies seen in all olivine–pigeonite ureilites), whereas the Warren and Kallemeyn (1992) mineralogy produces positive Eu anomalies

lies for $n > 2$. This difference is due to the much smaller amount of plagioclase in our composition, and its earlier exhaustion from the residue. In both cases, results essentially converge for $n > 75$, approaching perfect fractional melting. The two sets of results, however, lead to similar conclusions. Compared to the CI-normalized REE patterns for Kenna, both suggest that in an incremental batch melting model, only a small number of steps of melt extraction could have been involved (at most 2 for our melting sequence). Results obtained for other selections of distribution coefficients (within the uncertainties in Fig. 15) are similar in this respect. Thus, we conclude that in an incremental batch melting model, REE in Kenna are not consistent with fractional melting.

5.5. Disequilibrium melting

Incremental batch melting is an equilibrium model. It assumes that equilibrium partitioning occurs between melt and residue even in the case of perfect fractional melting ($n \rightarrow \infty$) where each infinitesimal amount of melt produced is extracted from the residue instantly. Equilibrium

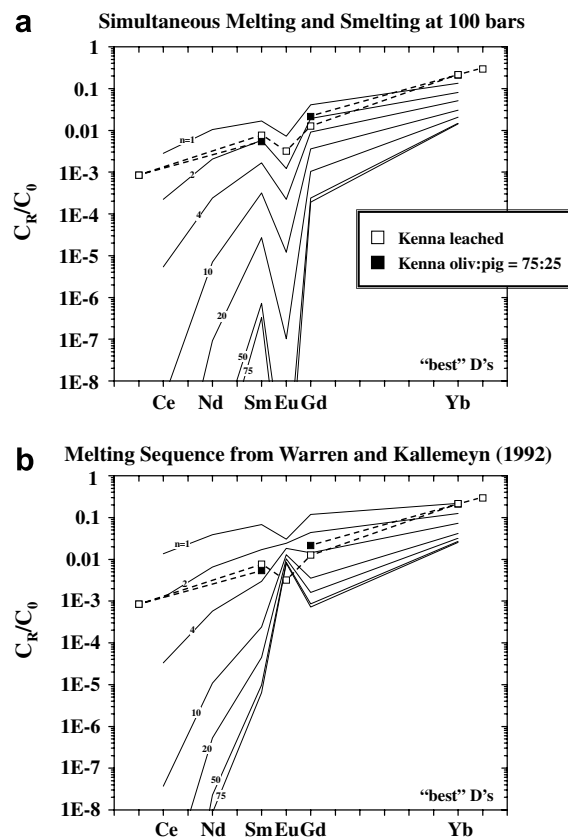


Fig. 16. Results of REE modelling, using the “best” set of distribution coefficients (solid squares in Fig. 15) for (a) the 100 bar simultaneous melting and smelting sequence derived in this work (Fig. 8a) and (b) the mineralogy and melting sequence of Warren and Kallemeyn (1992). The model is incremental batch melting, where n = the number of equal-sized steps of melt extraction. Most reliable REE patterns for residual ureilites (Kenna, representing one of the deepest source regions sampled) shown for comparison.

partitioning between minerals and melt may not be achieved during partial melting if the rate of diffusion in the minerals is slow compared with the rate of melting (Van Orman et al., 2002). In this situation, incompatible elements are held within the solid at levels greater than their equilibrium partition coefficients imply, because they are unable to escape efficiently from the interiors of mineral grains. Thus, as the degree of disequilibrium increases, the effective partition coefficient tends toward one. Rare earth elements are fractionated from one another less efficiently under disequilibrium conditions, and the composition of the solid residue produced by disequilibrium fractional melting may resemble that produced by equilibrium batch melting (Van Orman et al., 2002). Because the timescale for melting of the UPB is likely to have been on the order of a few million years or less (Wilson et al., 2006), similar to the timescales considered by Van Orman et al. (2002), it is reasonable to consider whether disequilibrium may have been important during melting of the UPB and to evaluate its possible influence on the REE composition of the solid residue. The clearest evidence for diffusion-limited REE exchange during melting would be frozen-in diffusion profiles in the residual minerals. Such profiles have not been observed in ureilites (Guan and Crozaz, 2000). However, ureilites show abundant evidence for long duration equilibration at high temperatures (Mittlefehldt et al., 1998), which may have erased any diffusion profiles developed during partial melting.

Here, REE patterns for the final residue of disequilibrium near-fractional melting on the UPB are calculated for a range of melting timescales, using a modified version of the model described by Van Orman et al. (2002). The model treats an end-member case in which the redistribution of elements between minerals and melt is controlled only by diffusion in the minerals. A variety of recrystallization and dissolution/precipitation processes may short-circuit solid-state diffusion, enhancing the rate of mineral-melt exchange. If such processes were active during melting of the UPB, the distribution of trace elements would be intermediate between the diffusion-controlled scenario considered here and the equilibrium distribution models discussed above. Van Orman et al. (2002) considered melting in response to adiabatic decompression, with pressure and temperature decreasing as melting proceeds. Here, melting is considered to take place by heating at constant pressure (100 bars). For simplicity the temperature is assumed to increase linearly with time. Although this is not realistic, the results are similar to those obtained using more realistic thermal histories based on the calculations of Wilson et al. (2006), for the same total timescale of melting. The total melt fraction increases with temperature according to the 100 bar curve shown in Fig. 7b, and mineral proportions as a function of the total melt fraction follow the curves shown in Fig. 8a. Prior to the onset of melting, REE are partitioned between augite and plagioclase according to the ratio of their mineral/melt equilibrium partition coefficients. Olivine is a minor host of the REE and is thus ignored in these simulations. Augite and plagioclase grains are approximated as spheres, and the number of grains is assumed to remain constant as melting

proceeds, so that the grain radii decrease with the 1/3 power of the mineral's volume in the residue. As melting proceeds, the instantaneous melts that are produced equilibrate with the surfaces of augite and plagioclase grains, and REE are transferred from mineral interiors to the melt to the extent that they are able to diffuse out of the grains in the time available.

The diffusion coefficients for trivalent REE in plagioclase used in the simulations were calculated as functions of temperature using the experimentally determined Arrhenius expressions for labradorite given by Cherniak (2003). Diffusion coefficients of trivalent REE in augite were calculated as functions of both temperature and oxygen fugacity using the experimentally determined expressions of by Van Orman et al. (2001) for natural diopside. No experimental data are available for diffusion of Eu^{2+} in plagioclase or augite, so data for Pb^{2+} , which has the same charge and similar ionic radius, were used as a proxy. The Pb^{2+} diffusion data of Cherniak (1995) were used for plagioclase, and the Cherniak (2001) Cr-diopside data were used for augite. Simulations performed using experimental data for Sr^{2+} in labradorite (Cherniak and Watson, 1994), and Eu^{2+} in orthopyroxene (Cherniak and Liang, 2007) instead as proxies for Eu^{2+} diffusion in plagioclase and augite, respectively, gave similar results. Pigeonite begins to crystallize late in the melting/smelting sequence, after ~20% melting. No diffusion data are available for the REE in pigeonite, but the growth of pigeonite is so rapid (Fig. 8a) and REE diffusion in other pyroxenes so slow (Van Orman et al., 2001; Cherniak and Liang, 2007) that diffusive transfer between the melt and growing pigeonite is assumed to be negligible. In other words, uptake of the REE by pigeonite is treated as a fractional process, in which each increment of crystallizing pigeonite is in equilibrium with the instantaneous melt produced at that

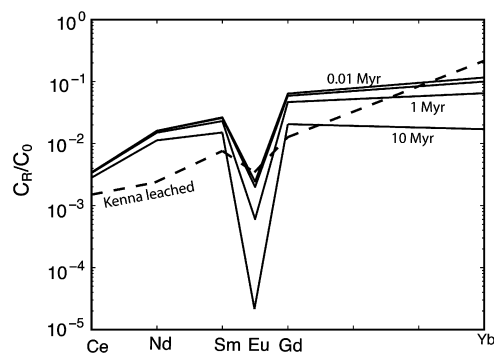


Fig. 17. Results of REE disequilibrium melting model. The model is for near-fractional melting with diffusion-controlled chemical exchange, slightly modified from that of Van Orman et al. (2002) as described in the text. A small amount of melt (0.1%) remains with the residue as melting proceeds, while the rest is extracted and undergoes no further interaction with the residual minerals. Augite and plagioclase grains are spheres with initial radii of 1 mm. Black curves show REE patterns in the residual solid after 30% melting (just after augite is exhausted from the residue) for four different total melting times, from 0.01 to 10 Myr. Kenna leached residue (dashed line) shown for comparison.

time and undergoes no subsequent exchange with melts produced later.

Fig. 17 shows REE patterns in the solid residue of disequilibrium near-fractional melting, just after the exhaustion of augite. The different patterns correspond to different melting rates, with the total melting time varying between 0.01 and 10 Myr. Although the melting process modelled is nearly fractional, with only 0.1% melt remaining in the solid residue, the REE are retained in the solid at relatively high concentrations because slow diffusion in the minerals prevents them from escaping efficiently as melting proceeds. The slower the melting rate, the more time is available for REE to diffuse into the melt; thus, with increasing melting time the REE concentrations in the residue decrease. The heavier trivalent REE, and divalent Eu especially, decrease more rapidly in the residue as the melting time increases because they diffuse more rapidly than the lighter REE. Diffusion of the light REE is slow enough to retain these elements in the residue at levels many orders of magnitude higher than they would be if equilibrium partitioning were attained, even when the melting time is as long as 10 Myr. When the melting time is shorter than ~ 0.1 Myr, there is very little diffusive exchange between minerals and melt, and the change in REE composition during melting is due almost entirely to changes in the mineral proportions. If melting were modal, with all minerals entering the melt in proportion to their abundance in the solid, the REE pattern in the residue would remain unchanged (flat) during melting. Instead, in these simulations plagioclase and augite enter the melt preferentially, carrying their complement of REE with them, and thus the REE concentrations in the solid decrease significantly as melting proceeds even when there is no diffusive exchange between minerals and melt. In the simulations shown in Fig. 17, the mineral grains were assumed to be 1 mm in radius initially. Larger grains would lead to less efficient diffusive exchange (and generally higher REE abundances in the residual solid), and smaller grains would allow a greater degree of exchange (and lower REE abundances). Because the diffusion length scales with the square root of time, decreasing the square of the grain size is equivalent to increasing the melting time by the same factor. For example, the REE pattern for 100- μm grains with a melting time of 0.1 Myr is the same as the REE pattern for 1 mm grains with a melting time of 10 Myr.

Fig. 17 shows that for a reasonable range of melting conditions on the UPB, the REE pattern of the residual solid may be controlled to a large extent by disequilibrium effects. Under these conditions, the predicted REE patterns for nearly perfect fractional melt extraction overlap the REE pattern of the leached Kenna sample, and clearly provide a much better match than the equilibrium model (Fig. 16). The calculated patterns are not a perfect match for Kenna, but the discrepancies are not fatally large. Yb and Eu concentrations (Fig. 17) tend to be lower than in Kenna, but for Yb the discrepancy would decrease by including olivine, which may hold a significant fraction of heavy REE, in the model. For Eu, the discrepancy may reflect a poor understanding of the diffusion kinetics: Despite differences in detail, Fig. 17 shows that the REE patterns in residual ureilites are consistent with efficient, fractional melt extraction, and do not re-

quire that a large melt fraction remain with the residue on the UPB.

6. FRACTIONAL EXTRACTION OF METALLIC MELTS AND DISEQUILIBRIUM PARTITIONING OF SIDEROPHILE ELEMENTS

The results of our work strongly support the idea that extraction of silicate melts on the UPB was fractional, and that disequilibrium partitioning of trace elements during this process determined their concentrations in the ureilitic residues. These results may also be applicable to metallic melts on the UPB, and in particular may help in removing one of the extant obstructants to the smelting model (Mittlefehldt et al., 2005; Warren and Huber, 2006). The smelting reaction implies formation of significant amounts of metal, in proportion to increase in *mg* of silicates. For example, ~ 11 wt% metal would be formed in shifting *mg* over the range (Fo 75–95) of ureilites (Warren and Huber, 2006). In our model, the total amount of metal produced would be even higher, since we assume that all source regions were originally *mg* ~ 62 . However, ureilites have metal contents that are uniformly low (at most $\sim 5\%$, more typically ≤ 1 –2%), and are not correlated with *mg* of silicates. Thus, if the smelting model is essentially correct, then most of the metal produced by smelting must have been removed from the silicate residues. Metal produced by smelting is likely to have been lost in the form of melt, since in the temperature range over which smelting occurred it should have been saturated with C and S and thus largely liquid. This is supported by the observation that ureilite siderophile element abundances are correlated with solid metal/liquid metal partition coefficients (Goodrich et al., 1987; Janssens et al., 1987; Jones and Goodrich, 1989; Spitz and Boynton, 1991; Rankenburg et al., 2005; Warren et al., 2006). The fate of this large quantity of metal, which is apparently not represented by any known meteorite, is not known (minor remnants of it may be found as 10–50 μm -sized cohenite-bearing metallic spherules included in olivine in a few ureilites: Goodrich and Berkley, 1986). Typically, density considerations would suggest that separated metal should sink. However, the smelting setting suggests that it may, instead, have migrated upwards due to inclusion of large amounts of gas, and erupted explosively to be lost to space (Keil and Wilson, 1993). Using the amounts of CO and CO₂ generated by smelting during each increment of silicate melting (Fig. 9c), together with the corresponding amounts of liquid iron produced by smelting, we have calculated the bulk density of the liquid iron + gas mixture, assuming that the gas was distributed uniformly throughout both of the liquid components. At the 30 bar pressure level, the bulk density of the iron + gas varies from ~ 30 to ~ 500 kg/m³ as smelting progresses; at the 100 bar pressure level it varies from ~ 100 to ~ 400 kg/m³. All of these densities are very much less than the ~ 3500 kg/m³ density of the unmelted host material, leading to a large buoyancy driving the fluids upward. Coalescence of the CO/CO₂ gas bubbles generated by smelting, as they rose through the liquid metal, would have led to the formation of

elongate gas bubbles (gas “slugs”), as happens under analogous conditions in basaltic silicate melts (Vergnolle and Jaupart, 1986). These slugs would have forced interstitial pockets of liquid metal upward, and would have left only a very thin veneer of this liquid on the silicate grains. Thus, we conclude that essentially all metallic melt produced by smelting would have been extracted very efficiently (in terms of both volume and speed), and its absence in the ureilite residues is not a mystery.

A related problem, however, is that ureilite trace siderophile element abundances are relatively undepleted (in the range of $0.1\text{--}1 \times \text{CI}$) compared with those in ultramafic rocks from differentiated parent bodies that are known to have experienced metal (core) segregation (Goodrich, 1992; Mittlefehldt et al., 1998). Moreover, they fail to show the negative correlation with *mg* that is predicted by smelting. Both Mittlefehldt et al. (2005) and Warren and Huber (2006) regard these observations as fatal to the model that smelting on the UPB was responsible for the variation in *mg* among monomict ureilites.

In contrast, we suggest that trace siderophile elements in ureilites might be consistent with the smelting model if their concentrations were established in a disequilibrium partitioning process. Our model implies that the amount of metal present in UPB source regions before smelting began was negligible, so that low-*T* mobilization/segregation of S-rich metallic melts, such as is commonly invoked for primitive achondrites (McCoy et al., 2006), was probably minor. Our calculated melt/smelt sequences, then, show when metal first appears in the melting sequence, for each depth (Fig. 8). As noted above, the temperatures at which this occurs are such that the majority of the metal formed must have been liquid. If extraction of metallic melts was a rapid, fractional process, then all metal would have been essentially removed the instant it formed. In this situation, the transfer of siderophile elements from the solid (where they initially reside solely in the silicate minerals) to the metallic melt is analogous to the transfer of REE to the silicate melt; the partitioning of siderophile elements is likely to be diffusion-limited, and disequilibrium effects may be important. Unfortunately, there are few experimental data on the diffusion of siderophile elements in the relevant silicates. Diffusion data do exist for Ni in olivine over a wide range of temperature and $f\text{O}_2$ (Petry et al., 2004). At conditions appropriate to smelting at 100 bars, Ni diffusion coefficients are in the range $6 \times 10^{-20}\text{--}2 \times 10^{-18} \text{ m}^2/\text{s}$, depending on the crystallographic orientation of olivine, and about an order of magnitude lower for smelting conditions at 30 bars. These values are somewhat higher than REE diffusivities in augite, but similar to or lower than REE diffusivities in plagioclase. Diffusion coefficients for Ni and other siderophiles are likely to be even lower in pyroxenes, given the generally sluggish diffusion kinetics in these minerals in comparison to olivine. Thus, based on the limited diffusion data available, at least some degree of disequilibrium seems likely. This would have had the effect of retaining siderophiles in the silicate residue above equilibrium levels, and thus might provide an explanation for the siderophile “overabundance” problem in ureilites.

ACKNOWLEDGMENTS

We thank J.L. Berkley, H. Connolly, A.M. Fioretti, T. Grove, J. Mikalopas, S. Singletary, K. Rankenburg, D.K. Ross, E.R.D. Scott, A.H. Treiman and M. Weisberg for helpful discussions. We especially thank John Longhi for his many efforts to improve the applicability of MAGPOX to ureilites. The comments of R.J. Walker, G. Benedix, Y. Liang and an anonymous reviewer are greatly appreciated. This work was supported by NASA Grants NNG05GH72G to C.A. Goodrich, NAG5-11591 to K. Keil, and NSF Grants 0337125 and 0322766 to J. Van Orman.

REFERENCES

- Allegre C. J., and Minster J. F. (1978) Quantitative models of trace element behavior in magmatic processes. *Earth Planet. Sci. Lett.* **38**, 1–25.
- Berkley J. L., and Jones J. H. (1982) Primary igneous carbon in ureilites: petrological implications. *Proc. Lunar Planet. Sci. Conf.* **13**, A353–A364.
- Bischoff A., Palme H., Spettel B., Clayton R. N., and Mayeda T. K. (1988) The chemical composition of dark inclusions from the Allende meteorite. *Lunar Planet. Sci.* **19**, 88–89.
- Boynton W. V., Starzyk P. M., and Schmitt R. A. (1976) Chemical evidence for the genesis of the ureilites, the achondrite Chassigny and the nakhlites. *Geochim. Cosmochim. Acta* **40**, 1439–1447.
- Cherniak D. J. (1995) Diffusion of lead in plagioclase and K-feldspar: an investigation using Rutherford backscattering and resonant nuclear reaction analysis. *Contrib. Mineral. Petrol.* **120**, 358–371.
- Cherniak D. J. (2001) Pb diffusion in Cr diopside, augite, and enstatite, and consideration of the dependence of cation diffusion in pyroxene on oxygen fugacity. *Chem. Geol.* **177**, 381–397.
- Cherniak D. J. (2003) REE diffusion in feldspar. *Chem. Geol.* **193**, 25–41.
- Cherniak D. J., and Liang Y. (2007) Rare earth element diffusion in natural enstatite. *Geochim. Cosmochim. Acta* **71**, 1324–1340.
- Cherniak D. J., and Watson E. B. (1994) A study of strontium diffusion in plagioclase using Rutherford backscattering spectroscopy. *Geochim. Cosmochim. Acta* **58**, 5179–5190.
- Clayton R. N., and Mayeda T. K. (1988) Formation of ureilites by nebular processes. *Geochim. Cosmochim. Acta* **52**, 1313–1318.
- Clayton R. N., and Mayeda T. K. (1996) Oxygen-isotope studies of achondrites. *Geochim. Cosmochim. Acta* **60**, 1919–2018.
- Cohen B. A., and Coker R. F. (2000) Modeling of liquid water on CM meteorite parent bodies and implications for amino acid racemization. *Icarus* **145**, 369–381.
- Cohen B. A., Goodrich C. A., and Keil K. (2004) Feldspathic clast populations in polymict ureilites: stalking the missing basalts from the ureilite parent body. *Geochim. Cosmochim. Acta* **68**, 4249–4266.
- Dohmen R., Chakraborty S., and Becker H. W. (2002) Si and O diffusion in olivine and implications for characterizing plastic flow in the mantle. *Geophys. Res. Lett.* **29**, Art. No. 2030.
- French B. M., and Eugster H. P. (1965) Experimental control of oxygen fugacities by graphite–gas equilibria. *J. Geophys. Res.* **70**, 1529–1539.
- Fruiland R. M., King E. A., and McKay D. S. (1978) Allende dark inclusions. *Proc. Lunar Planet. Sci. Conf.* **9**, 1305–1329.
- Ghiorso M. S., and Sack R. O. (1995) Chemical mass transfer in magmatic processes IV. A revised and internally consistent thermodynamic model for the interpolation and extrapolation of liquid–solid equilibria in magmatic systems at elevated

- temperatures and pressures. *Contrib. Mineral. Petrol.* **119**, 197–212.
- Goodrich C. A. (1992) Ureilites: a critical review. *Meteoritics* **27**, 327–352.
- Goodrich C. A. (1999) Are ureilites residues from partial melting of chondritic material? The answer from MAGPOX. *Meteorit. Planet. Sci.* **34**, 109–119.
- Goodrich C. A., and Berkley J. L. (1986) Primary magmatic carbon in ureilites: evidence from cohenite-bearing metallic spherules. *Geochim. Cosmochim. Acta* **50**, 681–691.
- Goodrich C. A., and Delaney J. S. (2000) Fe/Mg–Fe/Mn relations of meteorites and primary heterogeneity of primitive achondrite parent bodies. *Geochim. Cosmochim. Acta* **64**, 2255–2273.
- Goodrich C. A., and Lugmair G. W. (1995) Stalking the LREE-enriched component in ureilites. *Geochim. Cosmochim. Acta* **59**, 2609–2620.
- Goodrich C. A., Jones J. H., and Berkley J. L. (1987) Origin and evolution of the ureilite parent magmas: multi-stage igneous activity on a large parent body. *Geochim. Cosmochim. Acta* **51**, 2255–2273.
- Goodrich C. A., Lugmair G. W., Drake M. J., and Patchett P. J. (1995) Comment on “U–Th–Pb and Sm–Nd isotopic systematics of the Goalpara ureilite: resolution of terrestrial contamination” by N. Torigoye-Kita, K. Misawa, and M. Tatsumoto. *Geochim. Cosmochim. Acta* **59**, 4083–4085.
- Goodrich C. A., Krot A. N., Scott E. R. D., Taylor G. J., Fioretti A. M., and Keil K. (2002) Formation and evolution of the ureilite parent body and its offspring. *Lunar Planet. Sci.* **33**, #1379 (abstr.).
- Goodrich C. A., Scott E. R. D., and Fioretti A. M. (2004) Ureilitic breccias: clues to the petrologic structure and impact disruption of the ureilite parent asteroid. *Chemie de Erde* **64**, 283–327.
- Goodrich C. A., Wlotzka F., Ross D. K., and Bartoschewitz R. (2006) Northwest Africa 1500: plagioclase-bearing monomict ureilite or unique achondrite?. *Meteorit. Planet. Sci.* **41**, 925–952.
- Grady M. M., Wright I. P., Swart P. K., and Pillinger C. T. (1985) The carbon and nitrogen isotopic composition of ureilites: implications for their genesis. *Geochim. Cosmochim. Acta* **49**, 903–915.
- Grove T. L., and Bence A. E. (1977) Experimental study of pyroxene–liquid interaction in quartz–normative basalt 15597. *Proc. Lunar Sci. Conf.* **8**, 1549–1579.
- Grove T. L., and Juster T. C. (1989) Experimental investigations of low-Ca pyroxene stability and olivine–pyroxene–liquid equilibria at 1-atm in natural basaltic and andesitic liquids. *Contrib. Mineral. Petrol.* **103**, 287–305.
- Grutzeck M., Kridelbaugh S., and Weill D. (1974) The distribution of Sr and REE between diopside and silicate liquid. *Geophys. Res. Lett.* **1**, 273–275.
- Guan Y., and Crozaz G. (2000) Light rare earth element enrichments in ureilites: a detailed ion microprobe study. *Meteorit. Planet. Sci.* **35**, 131–144.
- Ikeda Y., and Prinz M. (2001) Magmatic inclusions and felsic clasts in the Dar al Gani 319 polymict ureilite. *Meteorit. Planet. Sci.* **36**, 481–499.
- Ikeda Y., Prinz M., and Nehru C. E. (2000) Lithic and mineral clasts in the Dar al Gani (DAG) 319 polymict ureilite. *Antarct. Meteorit. Res.* **13**, 177–221.
- Janssens M.-J., Hertogen J., Wolf R., Ebihara M., and Anders E. (1987) Ureilites—trace element clues to their origin. *Geochim. Cosmochim. Acta* **51**, 2275–2283.
- Johnson C. A., Prinz M., Weisberg M. K., Clayton R. N., and Mayeda T. K. (1990) Dark inclusions in Allende, Leoville, and Vigarano: evidence for nebular oxidation of CV3 constituents. *Geochim. Cosmochim. Acta* **54**, 819–830.
- Jones J. H. (1995) Experimental trace element partitioning. In *Rock Physics and Phase Relations. A Handbook of Physical Constants*. American Geophysical Union, Washington, DC, pp. 73–104.
- Jones J. H., and Goodrich C. A. (1989) Siderophile trace element partitioning in the Fe–Ni–C system: preliminary results with application to ureilite petrogenesis. *Meteoritics* **24**, 281–282 (abstr.).
- Kallemeyn G. W., and Warren P. H. (1994) Geochemistry of LEW 88774 and two other unusual ureilites. *Lunar Planet. Sci.* **25**, 663–664 (abstr.).
- Keil K., and Wilson L. (1993) Explosive volcanism and the compositions of cores of differentiated asteroids. *Earth Planet. Sci. Lett.* **117**, 111–124.
- Kita N. T., Ikeda Y., Togashi S., Liu Y., Morishita Y., and Weisberg M. K. (2004) Origin of ureilites inferred from a SIMS oxygen isotopic and trace element study of clasts in the Dar al Gani 319 polymict ureilite. *Geochim. Cosmochim. Acta* **68**, 4213–4235.
- Krot A. N., Scott E. R. D., and Zolensky M. E. (1995) Mineralogical and chemical modification of components in CV3 chondrites: nebular or asteroidal processing. *Meteoritics* **30**, 748–775.
- Krot A. N., Scott E. R. D., and Zolensky M. E. (1997) Origin of fayalitic olivine rims and lath-shaped matrix olivine in the CV3 chondrite Allende and its dark inclusions. *Meteorit. Planet. Sci.* **32**, 31–49.
- Krot A. N., Petaev M. I., Scott E. R. D., Choi B.-G., Zolensky M. E., and Keil K. (1998) Progressive alteration in CV3 chondrites: more evidence for asteroidal alteration. *Meteorit. Planet. Sci.* **33**, 1065–1085.
- Longhi J. (1991) Comparative liquidus equilibria of hypersthene-normative basalts at low pressure. *Am. Mineral.* **76**, 785–800.
- Longhi J., and Pan V. (1988) Phase equilibrium constraints on the howardite–eucrite–diogenite association. *Proc. Lunar Planet. Sci. Conf.* **18**, 459–470.
- McCoy T. J., Mittlefehldt D. W., and Wilson L. (2006) Asteroid Differentiation. In *Meteorites and the Early Solar System II* (eds. D. S. Lauretta and H. Y. McSween). University of Arizona Press, pp. 733–745.
- McKay G. A. (1986) Crystal/liquid partitioning of REE in basaltic systems: extreme fractionation of REE in olivine. *Geochim. Cosmochim. Acta* **50**, 69–79.
- McKay G., Wagstaff J., and Yang S.-R. (1986) Clinopyroxene REE distribution coefficients for shergottites: the REE content of the Shergotty melt. *Geochim. Cosmochim. Acta* **50**, 927–937.
- McKay G., Le L., and Wagstaff J. (1991) Constraints on the origin of the mare basalt europium anomaly: REE partition coefficients for pigeonite. *Lunar Planet. Sci.* **22**, 883–884 (abstr.).
- Mittlefehldt D. W., McCoy T. J., Goodrich C. A., and Kracher A. (1998) Non-chondritic meteorites from asteroidal bodies. In *Planetary Materials* (ed. J. J. Papike). Mineralogical Society of America. *Rev. Mineral.* **36**, 195 pp.
- Mittlefehldt D. W., Hudon P., and Galindo Jr., C. (2005) Petrology, geochemistry and genesis of ureilites. *Lunar Planet. Sci. XXXVI*. Lunar Planet. Inst., Houston. #1140 (abstr.).
- Nitsan U. (1974) Stability field of olivine with respect to oxidation and reduction. *J. Geophys. Res.* **79**, 706–711.
- Petry C., Chakraborty S., and Palme H. (2004) Experimental determination of Ni diffusion coefficients in olivine and their dependence on temperature, composition, oxygen fugacity, and crystallographic orientation. *Geochim. Cosmochim. Acta* **68**, 4179–4188.
- Rankenburg K., Brandon A. D., and Humayun M. (2005) Highly siderophile elements and osmium isotope systematics in ureilites: are the carbonaceous veins primary components? *Lunar Planet. Sci. XXXVI*. Lunar Planet. Inst., Houston. #1224 (abstr.).

- Russell S. S., Folco L., Grady M. M., Zolensky M. E., Jones R., Righter K., Zipfel J., and Grossman J. N. (2004) Meteoritical Bulletin, No. 88, 2004 July. *Meteorit. Planet. Sci.* **39**, A215–A272.
- Russell S. S., Zolensky M. E., Righter K., Folco L., Jones R., Connolly H. C., Grady M. M., and Grossman J. N. (2005) Meteoritical Bulletin, No. 89, 2005 September. *Meteorit. Planet. Sci.* **40**, A201–A263.
- Scott E. R. D., Taylor G. J., and Keil K. (1993) Origin of ureilite meteorites and implications for planetary accretion. *Geophys. Res. Lett.* **20**, 415–418.
- Singletary S. J., and Grove T. L. (2003) Early petrologic processes on the ureilite parent body. *Meteorit. Planet. Sci.* **38**, 95–108.
- Singletary S. J., and Grove T. L. (2006) Experimental constraints on ureilite petrogenesis. *Geochim. Cosmochim. Acta* **70**, 1291–1308.
- Sinha S. K., Sack R. O., and Lipschutz M. E. (1997) Ureilite meteorites: equilibration temperatures and smelting reactions. *Geochim. Cosmochim. Acta* **61**, 4242–4325.
- Spitz A. H., and Boynton W. V. (1991) Trace element analysis of ureilites: new constraints on their petrogenesis. *Geochim. Cosmochim. Acta* **55**, 3417–3430.
- Takeda H. (1989) Mineralogy of coexisting pyroxenes in magnesian ureilites and their formation conditions. *Earth Planet. Sci. Lett.* **93**, 181–194.
- Torigoye-Kita N., Misawa K., and Tatsumoto M. (1995a) U–Th–Pb and Sm–Nd isotopic systematics of the Goalpara ureilite: resolution of terrestrial contamination. *Geochim. Cosmochim. Acta* **59**, 381–390.
- Torigoye-Kita N., Misawa K., and Tatsumoto M. (1995b) Reply to the Comment by C.A. Goodrich, G.W. Lugmair, M.J. Drake and P.J. Patchett on “U–Th–Pb and Sm–Nd isotopic systematics of the Goalpara ureilite: resolution of terrestrial contamination”. *Geochim. Cosmochim. Acta* **59**, 4087–4091.
- Van Orman J. A., Grove T. L., and Shimizu N. (2001) Rare earth element diffusion in diopside: influence of temperature, pressure and ionic radius, and an elastic model for diffusion in silicates. *Contrib. Mineral. Petrol.* **141**, 687–703.
- Van Orman J. A., Grove T. L., and Shimizu N. (2002) Diffusive fractionation of trace elements during production and transport of melt in Earth’s upper mantle. *Earth Planet. Sci. Lett.* **198**, 93–112.
- Vergnolle S., and Jaupart C. (1986) Separated two-phase flow and basaltic eruptions. *J. Geophys. Res.* **91**, 12842–12860.
- Walker D., and Grove T. L. (1993) Ureilite smelting. *Meteoritics* **28**, 629–636.
- Warren P. H., and Huber H. (2006) Ureilite petrogenesis: a limited role for smelting during anatexis and catastrophic disruption. *Meteorit. Planet. Sci.* **41**, 835–849.
- Warren P. H., and Kallemeyn G. W. (1992) Explosive volcanism and the graphite–oxygen fugacity buffer on the parent asteroid(s) of the ureilite meteorites. *Icarus* **100**, 110–126.
- Warren P. H., Ulf-Møller F., Huber H., and Kallemeyn G. W. (2006) Siderophile geochemistry of ureilites: a record of early stages of planetesimal core formation. *Geochim. Cosmochim. Acta* **70**, 2104–2126.
- Williams R. J. (1972) Activity-composition relations in the fayalite–forsterite solid solution between 900 °C and 1300 °C at low pressures. *Earth Planet. Sci. Lett.* **15**, 296–300.
- Wilson L., and Keil K. (1991) Consequences of explosive eruptions on small solar system bodies: the case of the missing basalts on the aubrite parent body. *Earth Planet. Sci. Lett.* **104**, 505–512.
- Wilson L., Goodrich C. A., and Van Orman J. (2006) Thermal history and physics of melt extraction on the ureilite parent body. *Lunar Planet. Sci.* **37**, 12, Lunar Planet. Inst., Houston. #1177 (abstr.).

Associate editor: Richard J. Walker